1998

Modeling studies of the effects of wind forcing and thermohaline gradients on the California Current System

Batteen, Mary L.

PERGAMON

Deep-Sea Research II 45 (1998) 1507–1556

DEEP-SEA RESEARCH
PART II

Modeling studies of the effects of wind forcing and thermohaline gradients on the California Current System

Mary L. Batteen*, Philip W. Vance

Department of Oceanography, Naval Postgraduate School, Monterey, CA, 93943, USA

Received 23 June 1997; received in revised form 26 February 1998; accepted 13 March 1998

Abstract

This process-oriented study uses a high-resolution, multi-level, primitive equation model to study the combined effects of wind forcing and thermohaline gradients on the ocean circulation of the California Current System (CCS). The ocean circulation is generated by the model using a combination of climatological wind stress forcing and thermohaline gradients. In the first experiment, the effects of thermohaline gradients alone are evaluated; in the second experiment, previously conducted, the effects of wind forcing are isolated; while in the third experiment, the combined effects of wind forcing and thermohaline gradients are investigated. The results from the combined experiment show that even though the effects of wind forcing dominate the CCS, the additional effects of thermohaline gradients result in the following: the seasonal development of a poleward surface current and an equatorward undercurrent in the poleward end of the model region; an onshore geostrophic component, which results in a temperature front and stronger surface and subsurface currents between Cape Mendocino and Point Arena; and a region of maximum eddy kinetic energy inshore of ~ 125W between Cape Mendocino and Point Arena, associated with the temperature front. These model simulations are qualitatively similar to recent hydrographic, altimetric, drifter, and moored observations of the CCS. Published by Elsevier Science Ltd.

1. Introduction

Three types of water masses are found in the California Current System (CCS): Pacific sub-Arctic, North Pacific Central, and Southern waters (Hickey, 1998). The Pacific sub-Arctic water, characterized by low salinity and temperature and high

*Corresponding author. Fax: 001 831 656 2712; e-mail: batteen@oc.nps.navy.mil.

0967-0645/98/$ – see front matter Published by Elsevier Science Ltd.
PII: S0967-0645(98)00041-1

oxygen and nutrients, is advected equatorward in the CCS. North Pacific Central water, characterized by high salinity and temperature and low oxygen and nutrients, enters the CCS from the west. Southern water characterized by high salinity, temperature and nutrients, and low oxygen, enters the CCS from the south with the poleward undercurrent (Lynn and Simpson, 1987). The climatological mean CCS is the classical eastern boundary current (EBC) system, which consists of several large-scale currents (Fig. 1). The predominant flow is the California Current (CC), which, in the mean, is a broad ($\sim$ 1000 km), relatively slow ($\sim$ 10–30 cm/s), equatorward surface flow. It flows year-round, and extends to $\sim$ 500 m depth. The second basic flow is the California Undercurrent (CUC), which is a narrower ($\sim$ 10–40 km), relatively weak ($\sim$ 2–10 cm/s), poleward subsurface flow. It can vary seasonally and is strongest at $\sim$ 300 m depth. The third flow component is the Inshore Countercurrent (IC), known as the Davidson Current (DC) north of Point Conception. This is also a relatively weak ($\sim$ 5 cm/s) poleward flow, which is found during fall and winter at the surface and near the coast. There are other ICs known as the Southern California Countercurrent (SCC) to the south, and the Southern California Eddy (SCE) inshore of the Channel Islands within the California Bight (Hickey, 1979, 1998).

Recent observational studies have shown that the CCS is not the quiescent, stable system of currents with a well-defined, unchanging structure suggested by Fig. 1. Rather, the flow fluctuates greatly in both time and space (Chelton, 1984). There exist mesoscale meanders, eddies, filaments and jet-like surface currents, which are superimposed on the large-scale flow (e.g. Bernstein et al., 1977; Strub et al., 1991). The combination of these features has led to a new conceptualization of the CCS as

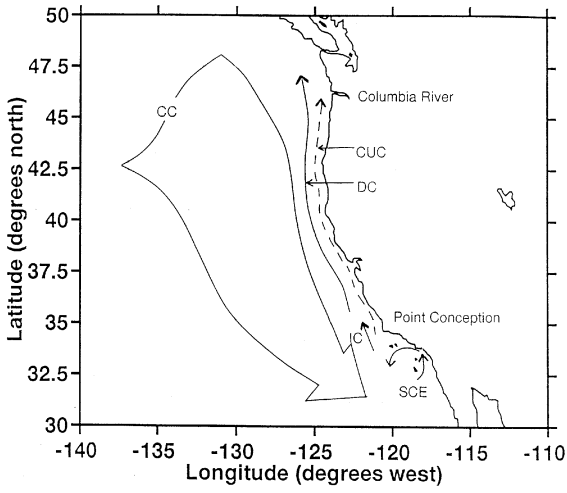

Fig. 1. Generalized circulation schematic of the classical climatological California Current System (CCS). The broad, slow surface equatorward California Countercurrent (CC) overlies the poleward California Undercurrent (CUC) along with the Inshore Countercurrent (IC), known as the Davidson Current (DC) north of Point Conception and as the Southern California Eddy (SCE) south of Point Conception.

a system of currents with filamented jets and mesoscale eddies modifying the mean flow (Mooers and Robinson, 1984).

The dynamical processes responsible for the generation and evolution of these intense and complex meander, eddy, and filament structures in the CCS have yet to be fully identified (Strub et al., 1991). A possible generative mechanism arises from the baroclinic and/or barotropic instability of the mean coastal CCS, which, during the upwelling season (approximately April through September) consists of the equatorward CC overlying the poleward CUC. This generative mechanism was explored first in modeling studies by Ikeda and Emery (1984), Ikeda et al. (1984a,b), and most recently by Haidvogel et al. (1991). In these studies, externally prescribed, longshore currents (representing the coastal jet and/or undercurrent) have been imposed and subsequently studied by analyzing the conditions that cause these currents to become unstable. The linear stability analysis of Ikeda et al. (1984a) has suggested that baroclinic instability can be an important process for generating meanders. Studies by Ikeda et al. (1984a,b), which incorporated the additional features of bumps to represent capes and ridges, have shown that the bumps can help trigger baroclinic instability, but the basic instability still results from the opposing alongshore currents. Haidvogel et al. (1991) prescribed an equatorial coastal jet in a model with bottom topography and irregular coastline geometry incorporated. Their results showed that the growth of instabilities was enhanced by coastline and/or topographic irregularities. An examination of these and other stability analyses (e.g. Pierce et al., 1991; Allen et al., 1991), laboratory modeling (e.g. Narimousa and Maxworthy, 1985, 1989), and numerical modeling (e.g. Walstad et al., 1991) of filament dynamics have led to the conclusion that finite amplitude instabilities of the CC can account for the origin and much of the behavior of observed filaments in the CCS (Brink and Cowles, 1991).

Another generative mechanism for the observed features in the CCS is wind forcing, which may be the most important mechanism for the generation of the currents as well as for the intense and complex meander, eddy, jet, and filament structures in the CCS. The wind forcing can set up the coastal currents, which subsequently can become unstable and lead to the formation of many of the features observed in the CCS. (In the modeling studies discussed above, the CC was prescribed rather than generated.) Satellite infrared imagery has shown evidence of these features during periods of winds favorable for upwelling, which suggests that wind forcing is a possible important mechanism for the formation of these features.

This generative mechanism in the CCS has been explored by Batteen et al. (1989), McCreary et al. (1991), Auad et al. (1991), and Pares-Sierra et al. (1993). In these model studies, externally imposed currents are not necessary; rather, the wind-forced models develop their own currents, which can subsequently become unstable. To isolate the role of wind forcing from the possible coupled effects of wind forcing and topographic variations, a flat bottom for the CCS has been used in all of the primitive equation (PE) process-oriented wind forcing studies.

Recent numerical modeling results from Batteen (1997) have built on the previous studies and have shown that both wind forcing and coastline irregularities are important mechanisms for the generation of many of the observed features of the CCS. In particular, the alongshore component of the wind stress has been shown to be

a key ingredient for generating realistic vertical and horizontal structures for the surface equatorward and subsurface poleward currents. With such structures the currents are baroclinically and barotropically unstable, resulting in the generation of meanders, filaments, and eddies. Irregularities in the coastline geometry also have been shown to be important for "anchoring" upwelling and filaments as well as enhancing the growth of meanders and eddies.

Seasonal dynamic height analyses by Batteen et al. (1995) have shown that the distribution of both temperature and salinity in the CCS can be important in defining the large-scale circulation. In particular, while temperature is, as expected, the major source of density variations, the mean variability of salinity has been shown to be responsible for a significant equatorward component along the coast of California and a strong offshore component adjacent to Baja. Based on this analysis, Batteen et al. (1995) concluded that, descriptively and dynamically, both temperature and salinity are essential to characterize the large-scale structure of the CCS accurately. An additional feature of the CCS is the seasonal strengthening and weakening seen in the dynamic height fields (Hickey, 1998).

Here we build on the previous studies of Batteen (1997) and Batteen et al. (1995) and ask the question what the combined wind forcing and thermohaline gradient effects are on the large-scale CCS circulation. To address this question three model experiments, one with climatological thermohaline gradients, one with climatological wind forcing, and one with both climatological wind forcing and thermohaline gradients, are run and compared with each other.

2. Model Description

2.1. Model equations

The numerical model in this study was originally used for a coarse resolution, closed basin by Haney (1974), and later adapted for eddy-resolving, limited EBC regions with open borders on the northern, western, and southern boundaries by Batteen et al. (1989), Batteen (1997), and Batteen and Butler (1998). The limited area EBC model is multi-level, uses non-adiabatic primitive equations on a beta-plane, and has both baroclinic and barotropic velocity components. The model is based on the hydrostatic, Boussinesq, and rigid lid approximations. The governing equations are as follows:

$$\frac{\mathrm{d}u}{\mathrm{d}t} = \frac{-1}{\rho_0}\frac{\partial \rho}{\partial x} + fv - A_M \nabla^4 u + K_M \frac{\partial^2 u}{\partial z^2}, \tag{1}$$

$$\frac{\mathrm{d}v}{\mathrm{d}t} = \frac{-1}{\rho_0}\frac{\partial \rho}{\partial y} + fu - A_M \nabla^4 v + K_M \frac{\partial^2 v}{\partial z^2}, \tag{2}$$

$$\frac{\partial u}{\partial x} + \frac{\partial v}{\partial y} + \frac{\partial w}{\partial z} = 0, \tag{3}$$

$$\frac{\partial \rho}{\partial z} = -\rho g, \tag{4}$$

$$\rho = \rho_0[1 - \alpha(T - T_0) + \beta(S - S_0)], \tag{5}$$

$$\frac{\mathrm{d}T}{\mathrm{d}t} = -A_H \nabla^4 T + K_H \frac{\partial^2 T}{\partial z^2}, \tag{6}$$

$$\frac{\mathrm{d}S}{\mathrm{d}t} = -A_H \nabla^4 S + K_H \frac{\partial^2 S}{\partial z^2}. \tag{7}$$

In the above equations, t is time, (x, y, z) is a right-handed Cartesian coordinate system with x pointing toward shore, y alongshore, and z upward. The corresponding velocity components are (u, v, w), T is temperature, S is salinity, ρ is density, and p is pressure. For the finite differencing, a space-staggered B-scheme (Arakawa and Lamb, 1977) is used in the horizontal. Batteen and Han (1981) have shown that this scheme is appropriate when the grid spacing is approximately on the same order as, or less than, the Rossby radius of deformation, which meets the criteria of this study. The horizontal grid spacing is 11 km in the alongshore direction and 8 km in the cross-shore direction, while the internal Rossby radius of deformation is $\sim$ 30 km. This horizontal grid resolution should allow realistic spatial resolution of mesoscale features in the CCS, which have typical wavelengths of the order of 100 km (Breaker and Mooers, 1986). In the vertical, the 10 layers are separated by constant z-levels of 13, 46, 98, 182, 316, 529, 870, 1416, 2283, and 3656 m. This spacing scheme concentrates more on the upper, dynamically active part of the ocean, above the thermocline.

The model domain (Fig. 2) is a rectangular region encompassing the west coast of the United States, from $\sim$ 35N to 47.5N (1408 km alongshore), and from $\sim$ 120W to 132.5W (1024 km cross-shore). The coastal boundaries of the model domain are closed, and have both the tangential and normal components of velocity set to zero. As in other wind-forced process oriented studies, bottom topography has been omitted to focus on the roles played by wind forcing and thermohaline gradients. (The additional inclusion of bottom topography and its effects on the CCS are considered a separate study). The constant depth used in the model is 4500 m.

A modified version of the radiation boundary conditions of Camerlengo and O'Brien (1980) is used for the open ocean domain boundaries to the north, south, and west. In particular, whether a boundary grid point is treated as an inflow point or an outflow point for a particular prognostic variable is determined by the sign of a dynamically computed effective group velocity. This group velocity is defined as the ratio of the local time derivative and the local space derivative normal to the boundary. If the boundary grid point is thereby determined to be an inflow point, then the value of the prognostic variable is set to its value at the previous timestep. If the boundary point is determined to be an outflow point, its value is set to that of the nearest interior point. Spatial smoothing is also applied with a 1-2-1 weighting window within five grid points ($\sim$ 50 km) of the open boundaries.

The model uses biharmonic lateral heat and momentum diffusion with the same choice of coefficients (i.e. 2.0×10^{17} cm^4 s^{-1}) as in Batteen et al. (1989). Holland (1978)

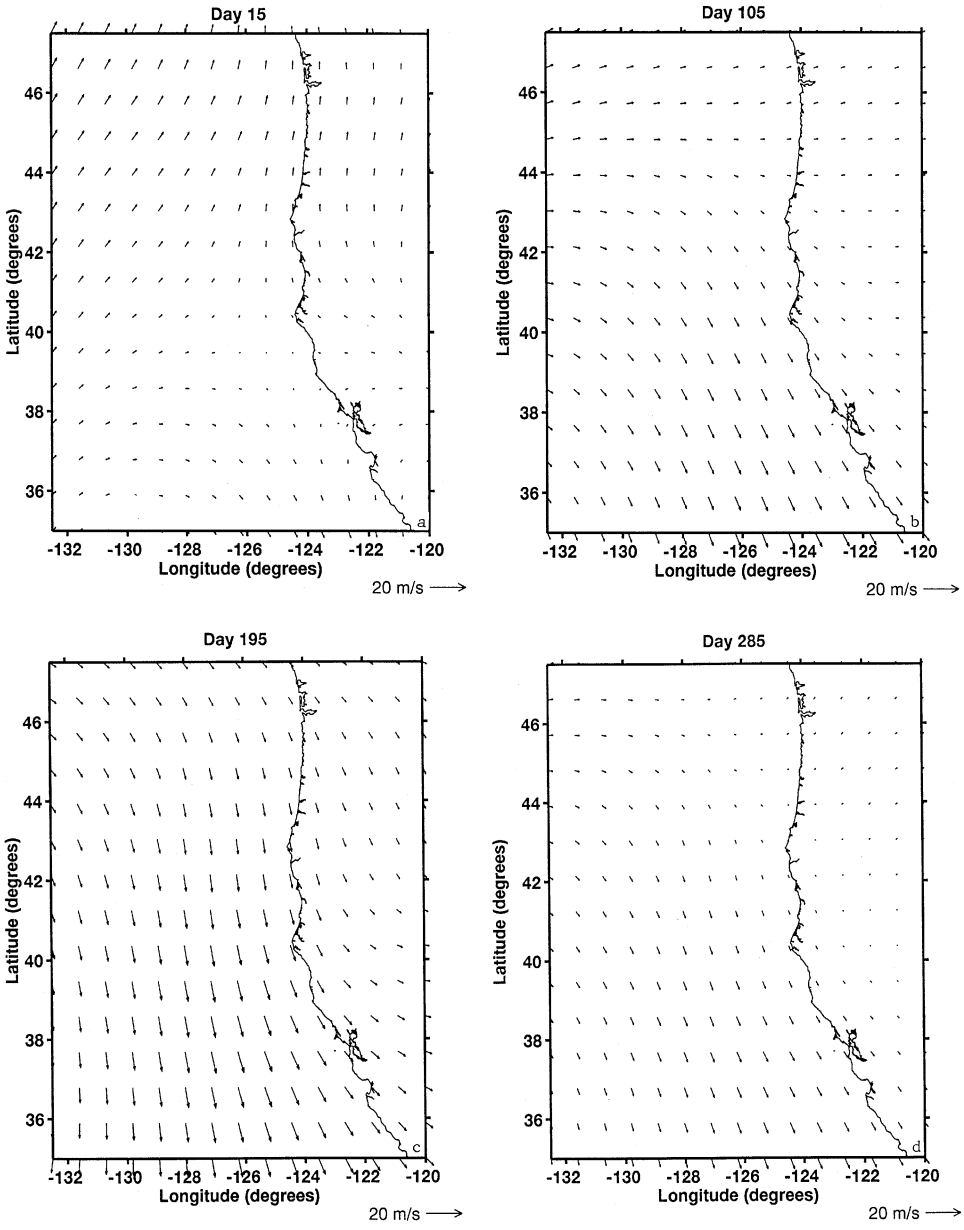

Fig. 2. Domain and climatological winds of the model for the California Current System (CCS) off the Western United States. The domain is bounded by 35N to 47.5N, 120W to 132.5W. The climatological (1980–1989) ECMWF winds used in Experiments 2 and 3 in m/s are shown here for (a) January, (b) April, (c) July, and (d) October. Maximum wind vector is 20 m/s.

showed that the highly scale-selective biharmonic diffusion acts predominantly on submesoscales, while Holland and Batteen (1986) found that baroclinic mesoscale processes can be damped by Laplacian lateral heat diffusion. As a result, the use of biharmonic lateral diffusion should allow mesoscale eddy generation via barotropic (horizontal shear) and/or baroclinic (vertical shear) instability mechanisms. As in Batteen et al. (1989), weak ($0.5\ cm^2\ s^{-1}$) vertical eddy viscosities and conductivity are used. Bottom stress is parameterized by a simplified quadratic drag law (Weatherly, 1972), as in Batteen et al. (1989).

The method of solution is straightforward with the rigid lid and flat bottom assumptions because the vertically integrated horizontal velocity is subsequently nondivergent. The vertical mean flow can be described by a streamfunction that can be predicted from the vorticity equation, while the vertical shear currents can be predicted after the vertical mean flow is subtracted from the original equations. The other variables, i.e. temperature, salinity, vertical velocity, and pressure, can be explicitly obtained from the thermodynamic energy equation (6), salinity equation (7), continuity equation (3), and hydrostatic equation (4), respectively (For more complete details on the method of solution, see Batteen, 1997).

2.2. Forcing conditions

In this study, when the effects of thermohaline gradients are explored (i.e. Experiments 1 and 3) on the CCS, seasonal temperature and salinity climatological conditions for the upper seven levels from Levitus et al. (1994) and Levitus and Boyer (1994) are used to initialize the model, and, once a day, to force the model at the western boundary. The seasonal temperature and salinity forcing conditions, which are initially assumed to be zonally homogeneous, are shown for two of the seven levels in Figure 3, for the northern (47.5°N) and southern (35°N) boundaries of the model domain. Since the lower three levels do not exhibit much horizontal variation, they are assumed to be constant for each level. The temperature values used for levels 8–10 are 2.56°C, 2.08°C, and 2.00°C. The salinity constant used for the lower three levels is 34.7.

While the temperatures to the south are warmer than those to the north above 1000 m depth, only the upper level temperature conditions (e.g. Fig. 3a) show significant seasonal variability with a temperature maximum in September and a temperature minimum in February throughout the whole region. Below around 150 m depth (e.g. Fig. 3b), both the seasonal temperature fluctuations and the temperature gradient weaken, as expected. In contrast the salinity conditions above 1000 m (Fig. 3), which in the upper levels show less (more) saline water to the north (south), have no significant seasonal cycle.

When the effects of seasonal wind forcing are explored (i.e., in Experiments 2 and 3), the model is forced with wind fields on a 2.5° by 2.5° grid from the European Center for Medium-Range Weather Forecasts (ECMWF) near-surface wind analyses (Trenberth et al., 1990). The monthly mean stresses based on twice daily wind analyses from 1980–1989 have been interpolated spatially to the 8 by 11 km model resolution and temporally to daily wind values.

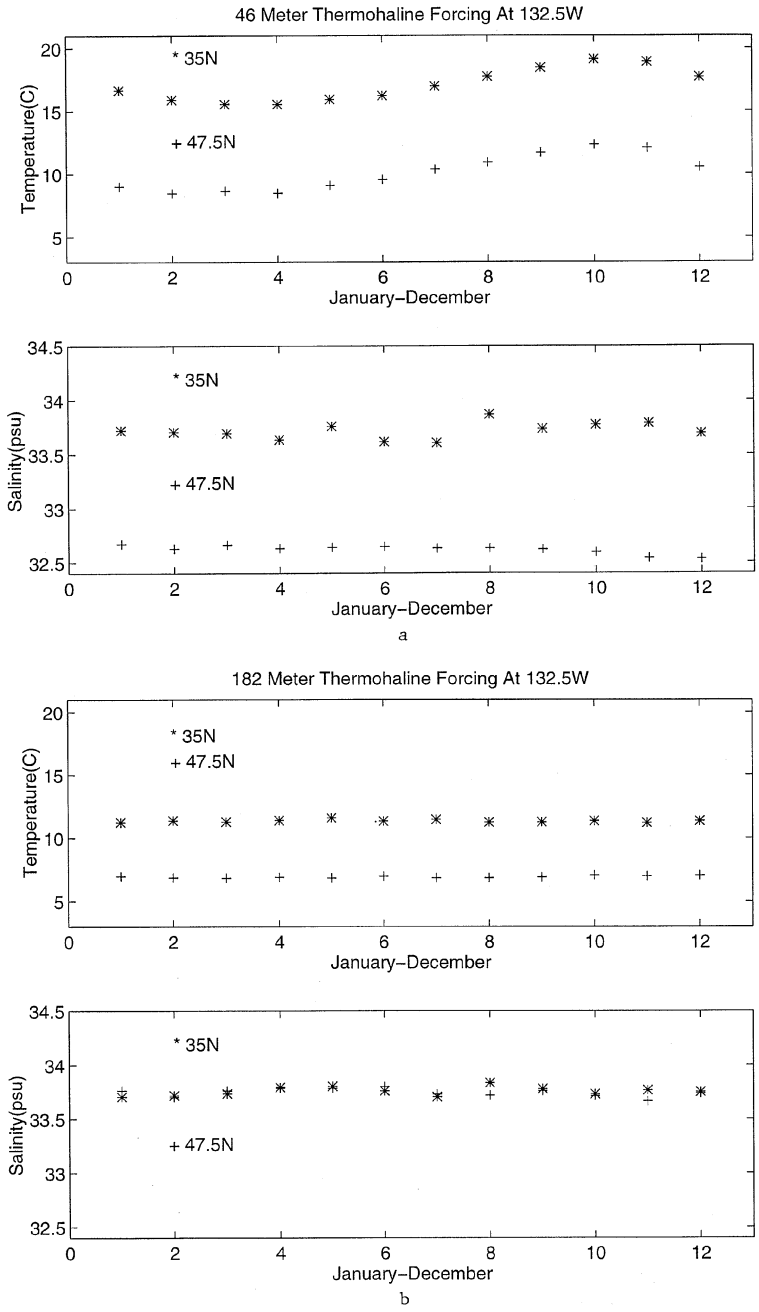

Fig. 3. Time series plot of monthly temperature and salinity fields used as seasonal forcing in Experiments 1 and 3. The '*' symbol represents data at 35N, 132.5W, while the ' + ' plot represents data at 47.5N, 132.5W for levels: (a) 46 m and (b) 182 m.

The wind forcing employed (Fig. 2) depicts the seasonal winds starting with January 15 (day 15). The atmospheric pressure pattern for January (Fig. 2a) has a low (i.e. the Aleutian Low) to the north and a high (i.e., the North Pacific High) to the south, which results in a wind divergence near 40°N. This pattern of poleward winds north of 40°N and equatorward winds to the south continues through February and March. During April (Fig. 2b) and May the divergence in the wind field migrates poleward. By June an equatorward component in the wind field is observed along the entire domain. The strongest equatorward winds are discernible from July (Fig. 2c) through August. By October (Fig. 2d) the winds start to weaken throughout the domain, and divergence in the wind field is observed in the north. This divergent wind pattern continues through November. By December the wind divergence has returned to $\sim 40°$N.

2.3. Experimental design

The design of the model experiments is as follows. Experiment 1 examines the model response to seasonal temperature and salinity gradients using the seasonal climatological conditions shown in Fig. 3. The model integrations start from a state of rest and, once a day, the model is updated for temperature and salinity at the western boundary.

In Experiment 2 the model is forced from rest with seasonal ECMWF winds. The initial mean stratification used is an exponential temperature profile with a vertical length scale of $h = 450$ m. The exact form is

$$T(z) = T_B + \Delta T\, e^{z/h}. \tag{8}$$

The approximation assumes $T_B = 2°$C to be the temperature at great depth. $\Delta T = 13°$C is the increase in temperature between the bottom of the ocean and the surface. This temperature profile is the same profile used by Batteen (1989, 1997) and Batteen et al. (1989) and was derived by Blumberg and Mellor (1987) from available CCS observations of the long-term, mean climatological temperature stratification for the CCS region as a whole

Like all major eastern boundary current systems, the CCS is a region of net annual gain (Nelson and Husby, 1983). This heat gain occurs because of relatively low cloud cover (compared with farther offshore), reduced latent heat flux, and downward sensible heat flux due to the presence of cold upwelled water during summer. To focus Experiment 2 on wind forcing as a possible mechanism for the generation of thermal variability in the CCS, the surface thermal forcing in the model was highly simplified. The solar radiation at the sea surface S_0, was specified to be the summer mean and CCS mean value from Nelson and Husby (1983). On the other hand, the sum of the net longwave radiation, latent, and sensible heat fluxes, Q_b, was computed during the model's experiments from standard bulk formulas (Haney et al., 1978) using the summer and CCS-mean value of the alongshore wind (above), cloud cover, relative humidity, air temperature, and model-predicted sea surface temperature. In Experiment 2, the initial sea surface temperature was chosen so that the total heat flux across the sea surface, $S_0 - Q_B$, was zero at the initial time. Therefore, the only surface heat flux forcing in the experiments was that which developed in Q_b as a result of (wind

forced) fluctuations in the sea surface temperature. As discussed in Haney (1985), such a surface thermal forcing damps the sea surface temperature fluctuations to the atmosphere on a time scale of the order of 100 days. Consequently, sea surface temperature fluctuations that develop due to wind forcing in Experiment 2 should be observed long before they are damped by the computed surface heat flux.

Experiment 3 combines the thermohaline gradients along the western boundary (Fig. 3) with the seasonal ECMWF wind forcing to study the model response to both types of forcing on the CCS. The model integrations start from a state of rest and, once a day, the model is updated with ECMWF winds and, at the western boundary, with temperature and salinity.

3. Results from model simulations

3.1. Experiment 1—seasonal temperature forcing and salinity gradients

3.1.1. Spin-up phase

As expected, when the temperature decreases poleward (Fig. 3), resulting in an increase of density poleward, the pressure gradient due to the temperature (density) gradient establishes an onshore geostrophic inflow from the interior ocean (Fig. 4). Because the initialized alongshore temperature field is not constant, the onshore flow varies between ~ 2 and 5 cm/s. As the flow approaches the eastern boundary, it turns and forms a poleward boundary current (e.g. Fig. 4a), which advects warm, less dense water from the equatorward end of the model domain. Because it is continually augmented downstream by additional onshore flow, the poleward current increases in magnitude towards the pole, so that by day 45 maximum velocities on the order of ~ 50 cm/s are observed near the poleward end of the model domain (Fig. 4b). As time progresses, the onshore geostrophic flow weakens in the southern region to ~ 1 and 2 cm/s. The poleward boundary current also weakens so that by day 180 (Fig. 4d) maximum speeds have decreased from ~ 50 cm/s at day 45 to ~ 20 cm/s. A minimum speed of ~ 10 cm/s is reached by day 255 (Fig. 4e), and is maintained throughout.

The longshore pressure gradient due to the temperature (density) gradient is sufficient to establish a coastal equatorward flow (e.g. see day 63 in Fig. 5). The strongest equatorward flow (~ 5 cm/s) is in the coastal, poleward end of the domain and is maintained throughout.

In addition to currents, eddies are generated in the CCS. By day 120 (Fig. 4c) anticyclonic eddies have developed between $\sim 39^\circ$N and 45°N. They subsequently intensify and propagate westward, as illustrated by following the position of the anticyclonic eddy between $\sim 43^\circ$N and 44°N in Figs. 4c–e. In time other anticyclonic eddies develop at the coast and subsequently propagate westward (not shown).

The surface (e.g. Fig. 4) and subsurface (e.g. Fig. 5) velocity fields superimposed on the density fields illustrate that away from the eddy generation region, the flow is predominantly parallel to the isopycnals, as expected for geostrophic flow. In the eddy generation region, i.e. in the poleward end of the model domain, there is significant advection of less dense water offshore by the anticyclonic eddies.

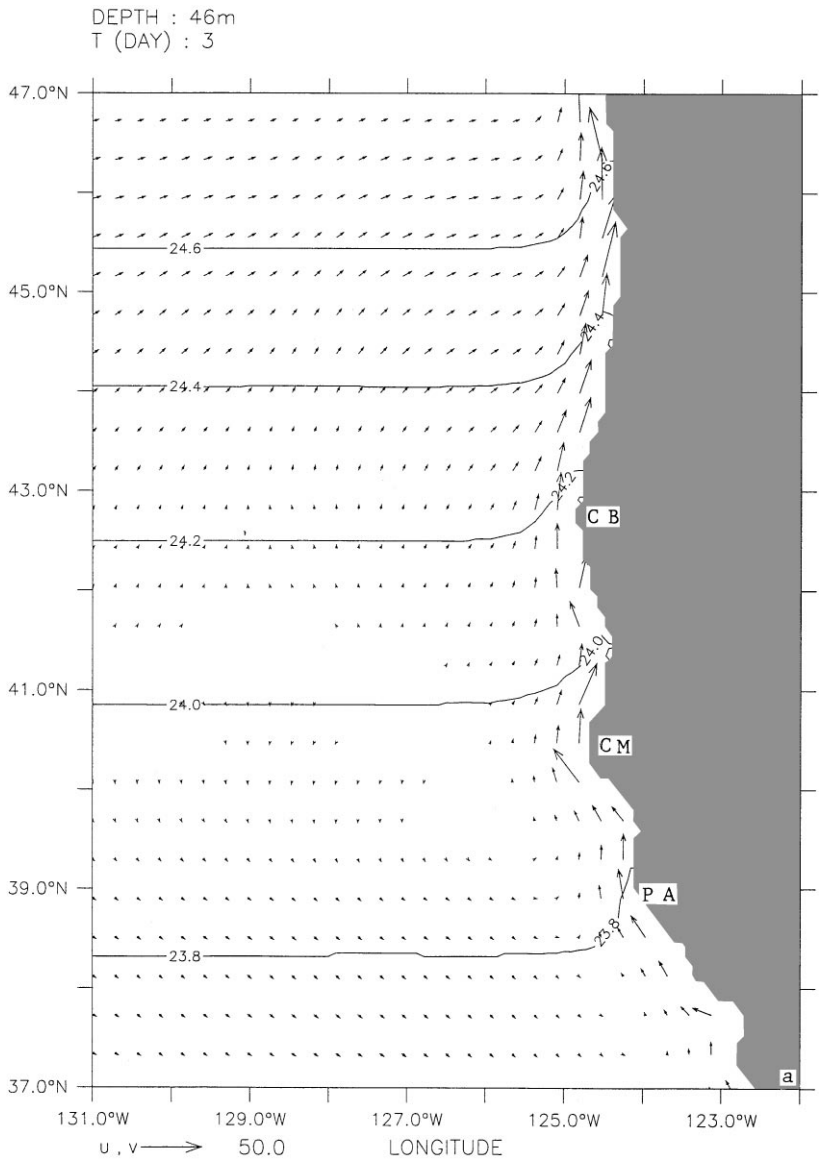

Fig. 4. Density contours and velocity vectors at 46 m depth for Experiment 1 at days (a) 3, (b) 45, (c) 120, (d) 180, and (e) 255. In all the velocity fields presented, to avoid clutter, velocity vectors are plotted every third (fourth) grid point in the cross-shore (alongshore) direction. Here and in the following figures, CB refers to Cape Blanco, CM to Cape Mendocino, and PA to Point Arena. Contour interval is 0.2 gm/cm^3; maximum velocity vector is 50 cm/s.

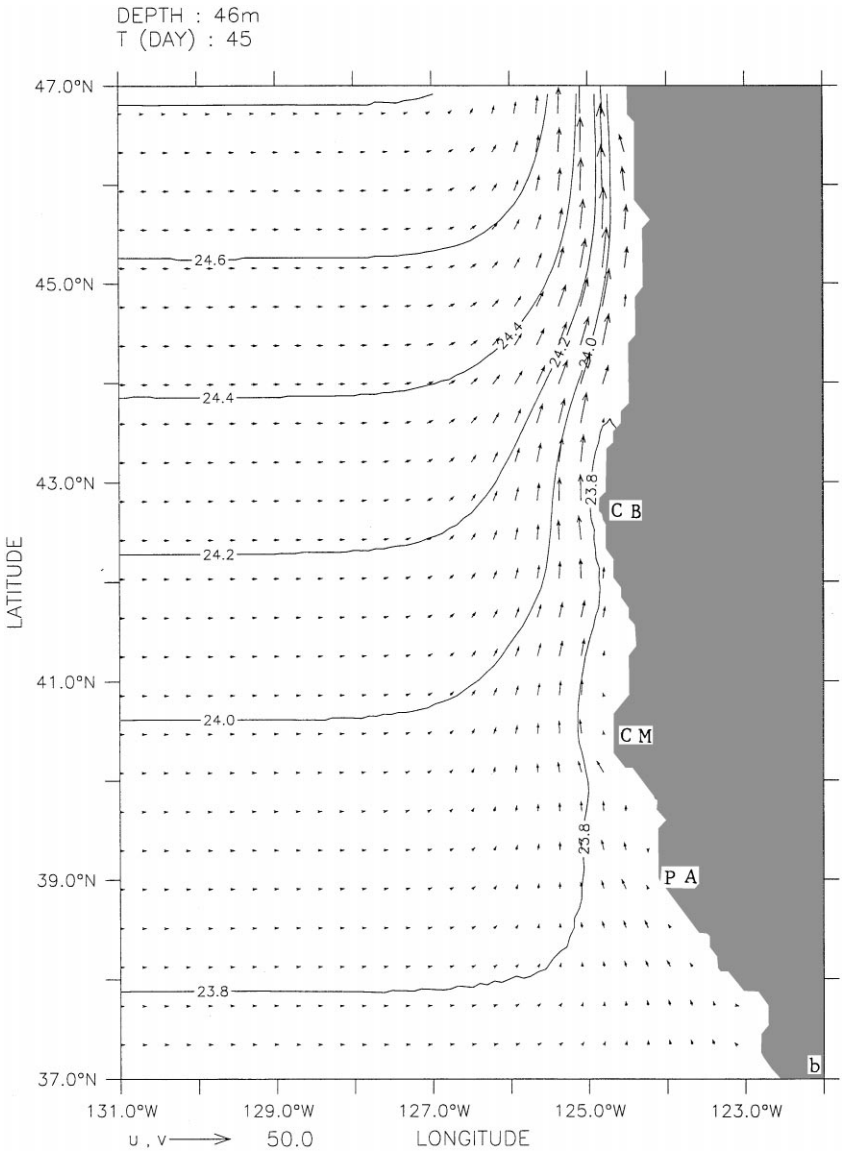

Fig. 4. Continued.

3.1.2. *Analysis of eddy propagation mechanisims*

The dynamical reasons for the generation and stability of eddies in Experiment 1 are examined using the energy techniques used and described by Batteen et al. (1992). From the energy transfer analysis, the location and magnitude of baroclinic and barotropic transfers can be found and examined to argue for the type of instability

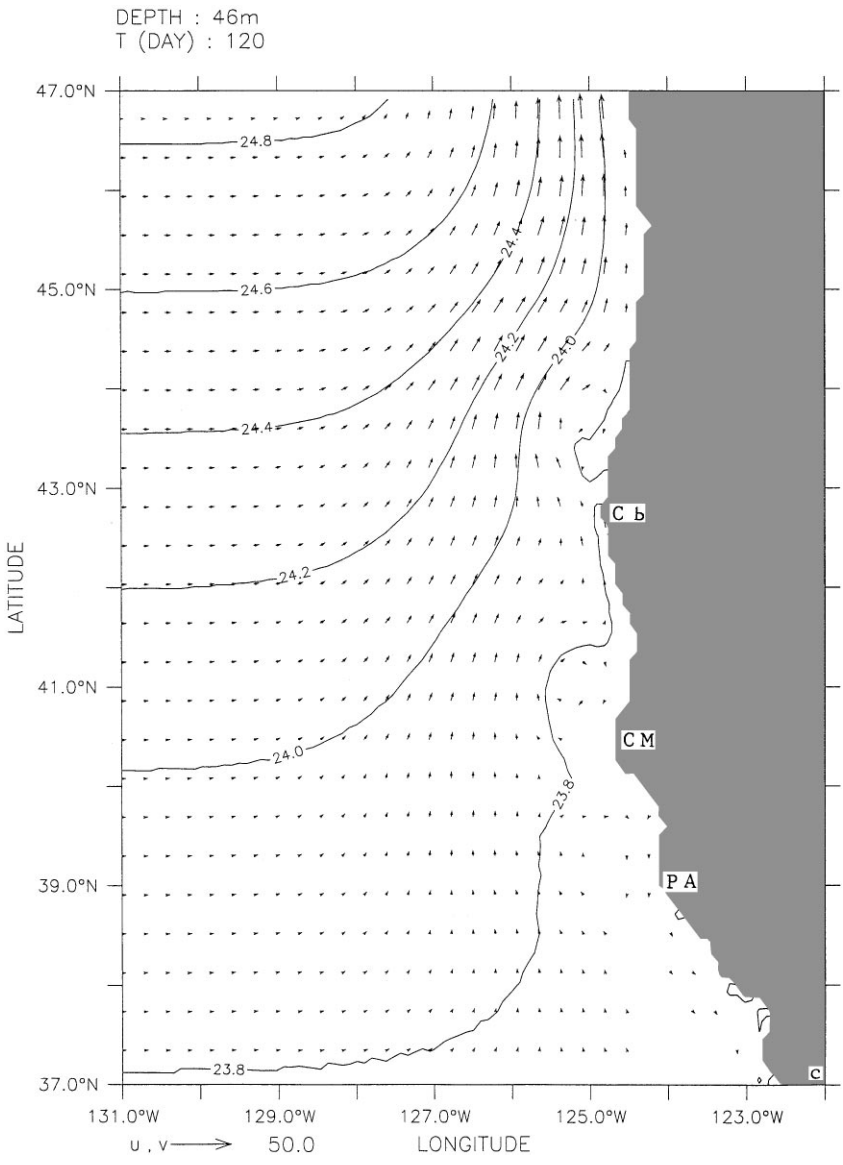

Fig. 4. Continued.

mechanism (e.g. barotropic, baroclinic, or mixed) which leads to the initial eddy generation.

Barotropic instability can result from horizontal shear in the currents, while baroclinic instability can result from vertical shear in the currents. As a result, both types of instability (mixed) can be present simultaneously. Energy transfer calculations, which consist of barotropic (mean kinetic energy to eddy kinetic energy) and

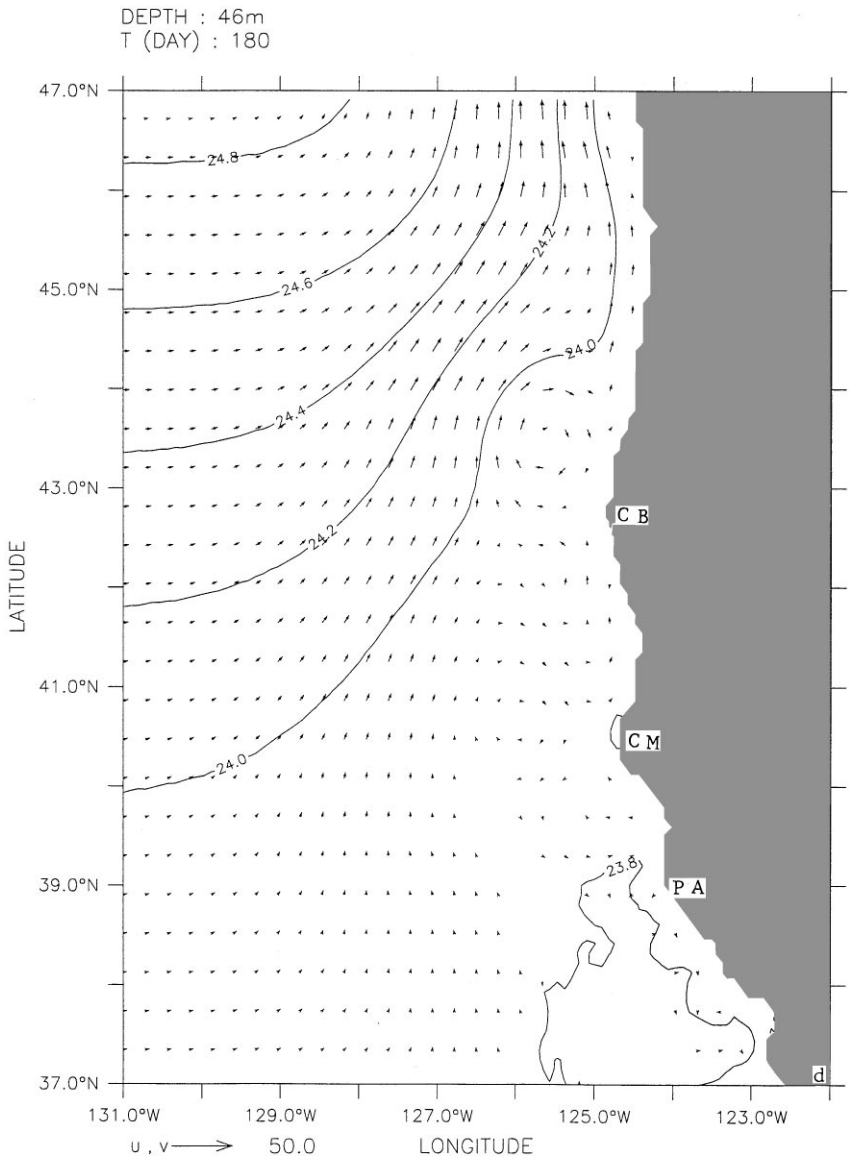

Fig. 4. Continued.

baroclinic (mean potential energy to eddy potential energy to eddy kinetic energy) components were performed for the time periods when the meanders and eddies developed, i.e. from days 90 to 120 and from 120 to 180.

Analysis of Fig. 6a shows both horizontal and vertical shear in the upper layer currents. Results of the energy transfer analyses for the time periods when the meanders and eddies developed (not shown) show that baroclinic instability is the

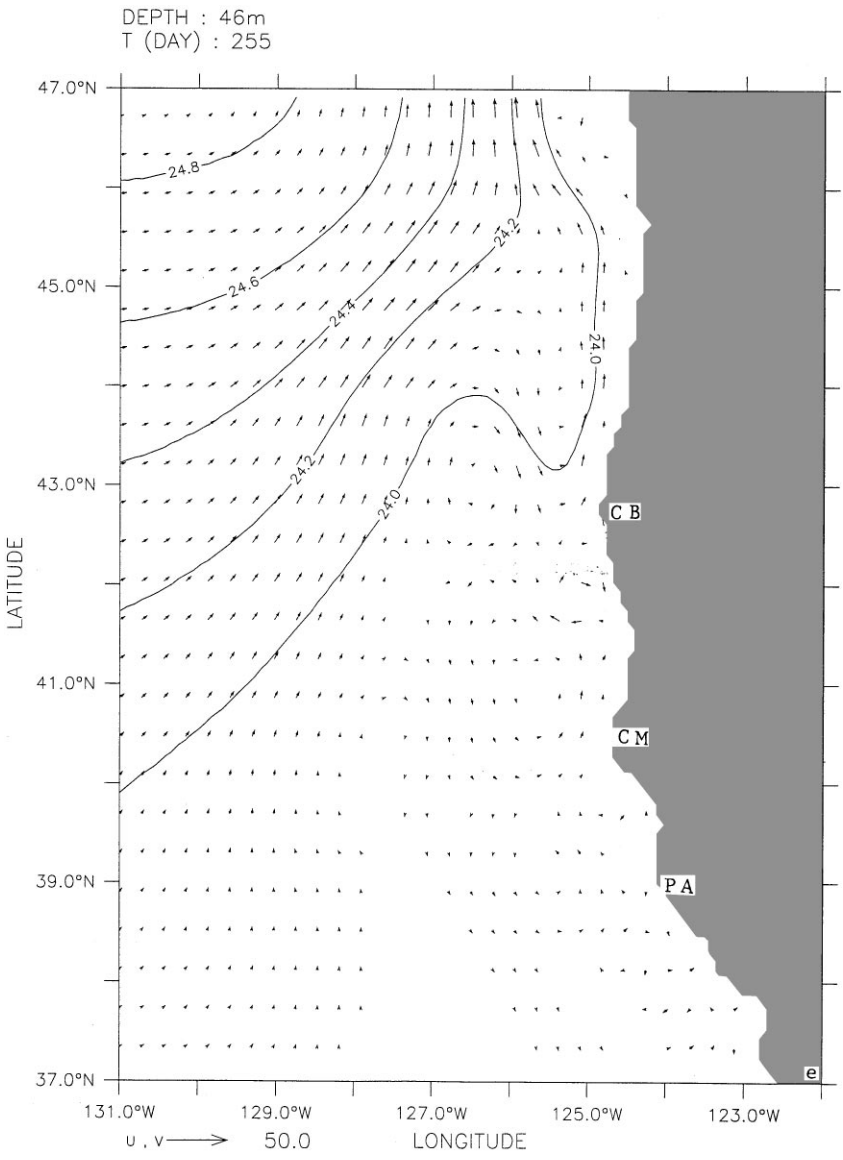

Fig. 4. Continued.

dominant type of instability mechanism which led to the anticyclonic eddy development near the coast north of $\sim 39°$N.

3.1.3. *Quasi-equilibrium phase*

Longer experimental runs show that the system has reached a quasi-steady state and that these features continue to be generated and maintained. Using the results of

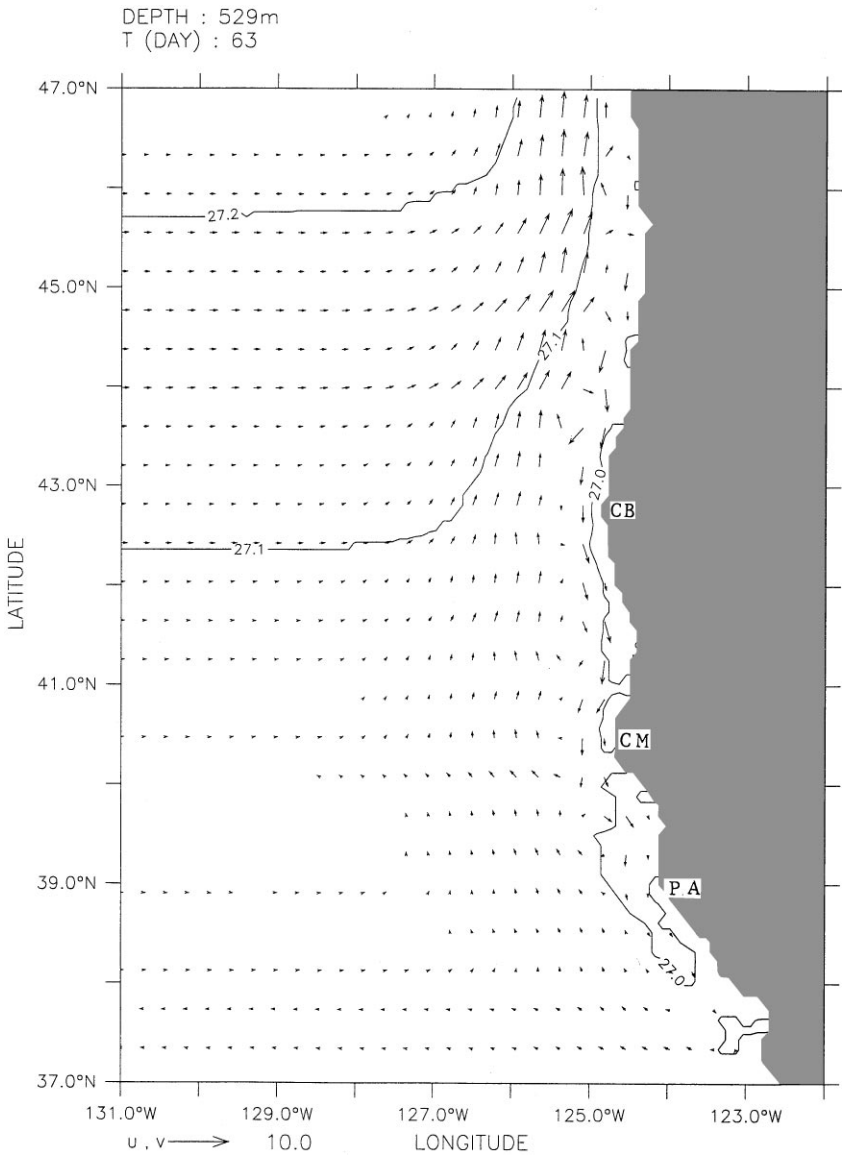

Fig. 5. Density contours and velocity vectors at 529 m depth for Experiment 1, day 63. Contour interval is 0.1 gm/cm^3; maximum velocity vector is 10 cm/s.

the longer experimental runs (i.e. year 3 of model simulation time), the model output is time-averaged every 3 days to see the structure of features in the CCS. As a result of geostrophic inflow due to the pressure gradient, both a poleward surface current and an equatorward undercurrent are generated. Fig. 6b shows the vertical structure of a coastal poleward surface current with a core velocity of $\sim$ 6–10 cm/s overlying

a coastal equatorward undercurrent with a core velocity of $\sim$1–2 cm/s between $\sim$150–300 m depth in the poleward part of the model domain.

The presence of both a poleward surface current and an equatorward undercurrent has been observed by Hickey (1979, 1998) off the coast of Washington. During the fall,

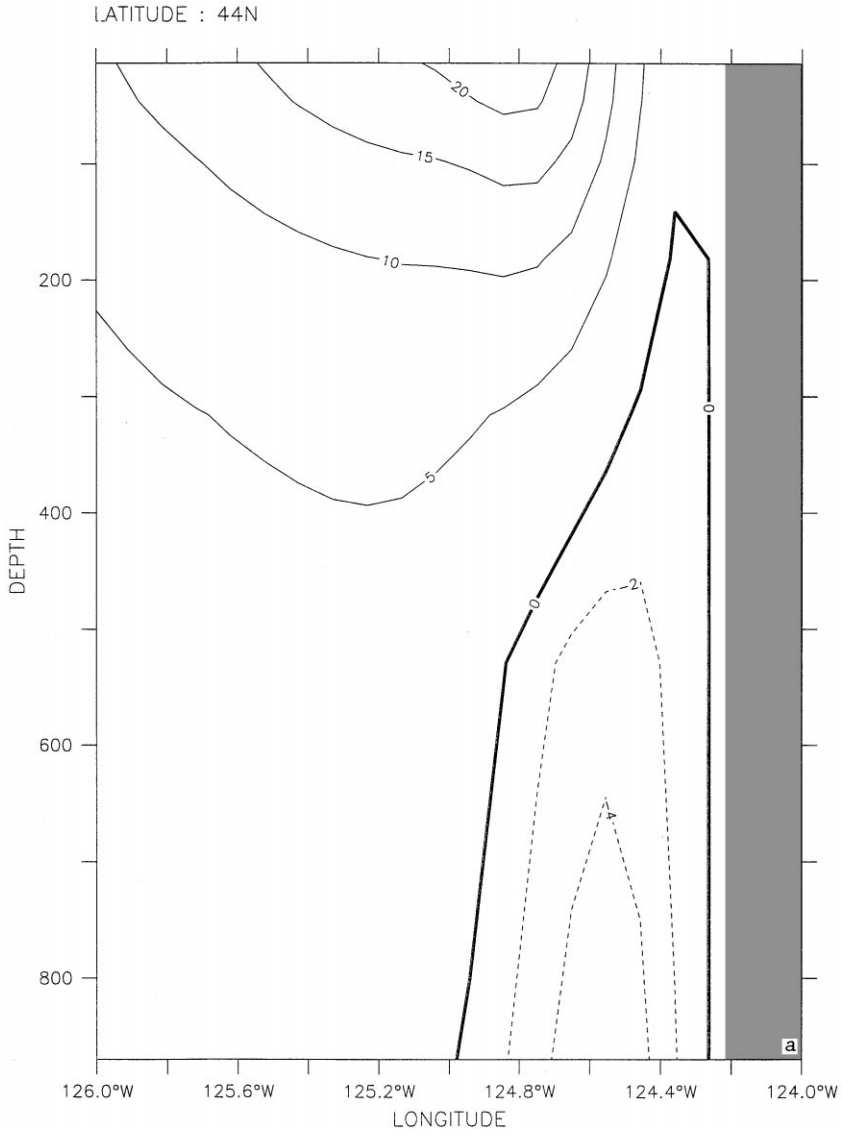

Fig. 6. Cross-shore sections of meridional velocity (v) at 44N in (a) and at 46N in (b) and (c) for Experiment 1 (a) at day 60 of model year 1, and time-averaged for days (b) 3–363 and (c) 270–363 of model year 3. Solid (dashed) lines denote poleward (equatorward) flow. Contour interval for poleward flow is 5 cm/s in (a) and (c) and 2 cm/s in (b). Contour interval for equatorward flow is 2 cm/s in (a) and 1 cm/s in (b) and (c).

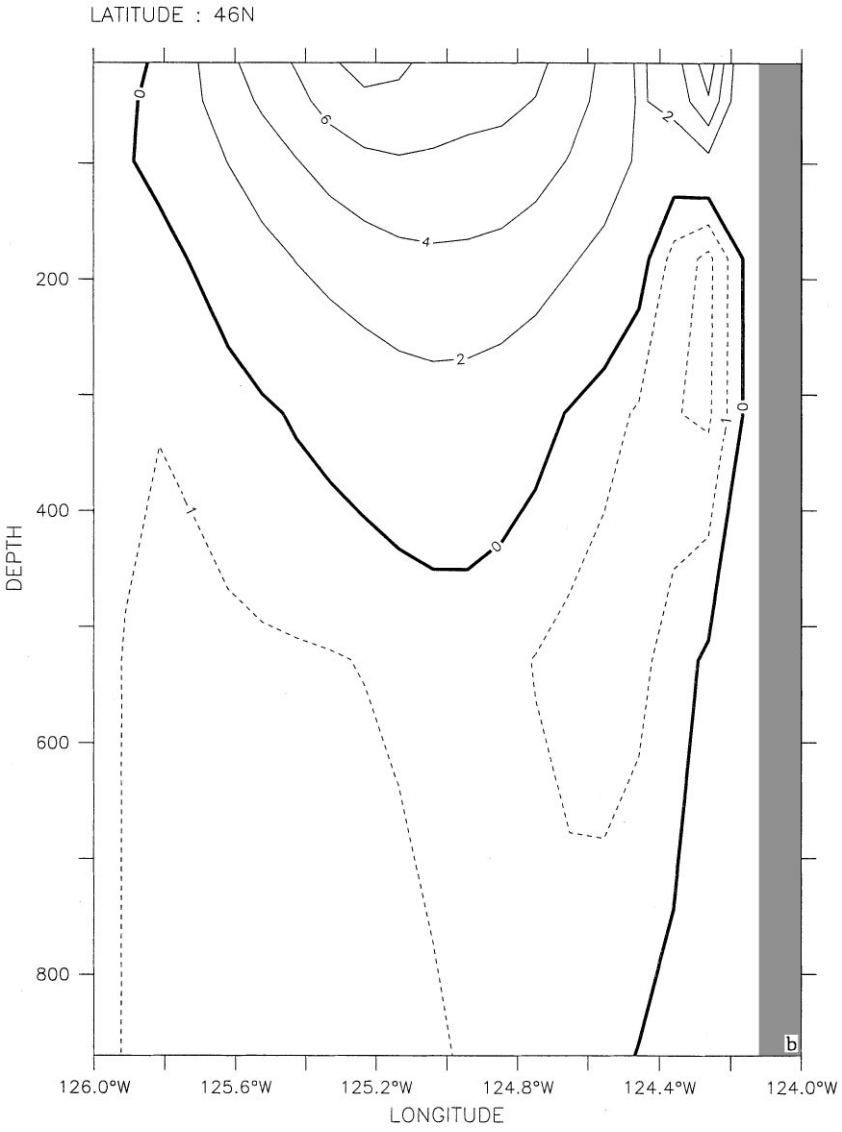

Fig. 6. Continued.

the coastal poleward surface current has been observed to have speeds of $\sim$ 5–20 cm/s and to occur above $\sim$ 150–300 m depth. The equatorward undercurrent has also been observed to have speeds of less than 10 cm/s, and to occur below $\sim$ 150–300 m depth. These observations are consistent with the results of the fall model simulations near the coast of Washington (e.g. Fig. 6c).

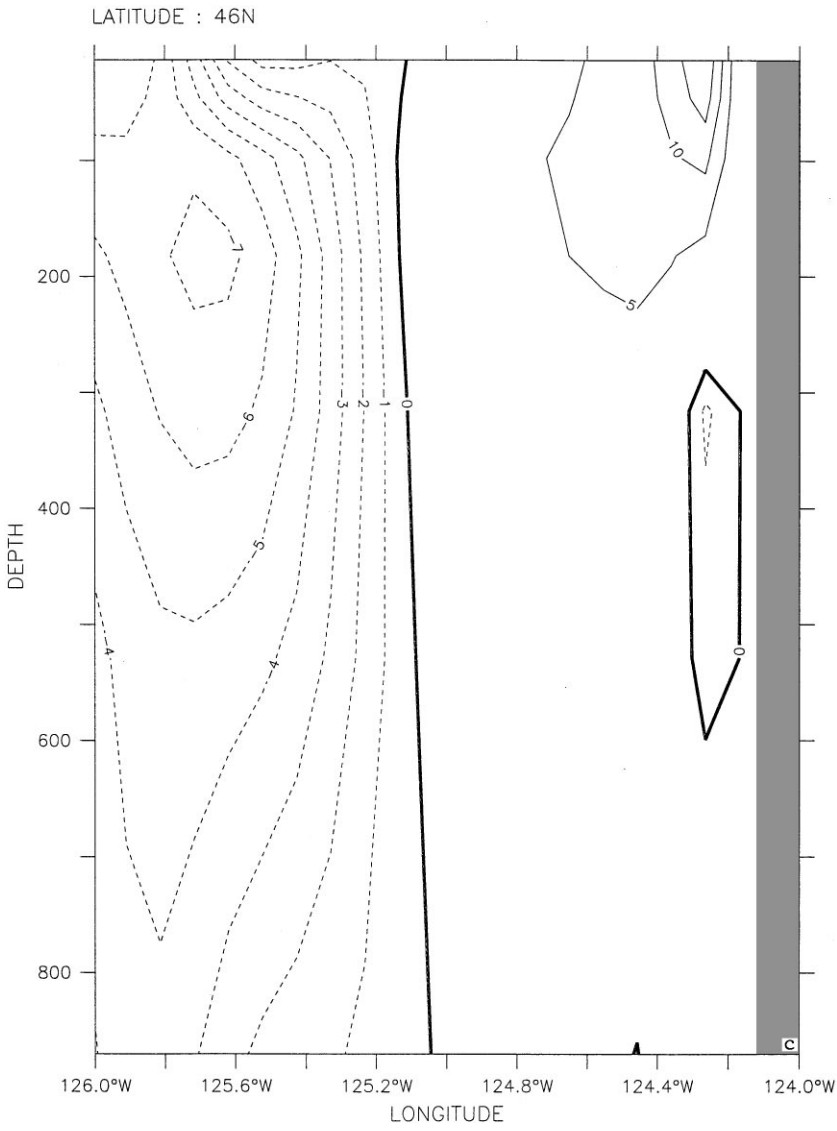

Fig. 6. Continued.

As in year 1 of the model simulation, anticyclonic eddies are generated in the coastal poleward end of the model domain. In time they intensify and propagate westward (not shown). Instability analysis (not shown) shows that as in model year 1, the eddies are due to baroclinic instability. The eddies tend to be $\sim$ 100 km in size and extend to depths of $\sim$ 300 m or deeper (not shown).

3.2. Experiment 2—seasonal wind forcing

3.2.1. Spin-up phase

Initially, the oceanic response to the climatological wind pattern (Fig. 2) used to force the model from rest, spins up linearly. In response to the prevailing poleward winds in the northern part of the model domain, a surface poleward coastal current of ~ 3 cm/s develops in the poleward end of the model domain within ~ 100 km of the coast. After being present for ~ 45 days, it retreats farther poleward following the migration of the Aleutian Low. As expected, equatorward wind forcing in the south results in an equatorward surface current (the CC) in the equatorward end of the model domain. By spring, with the arrival of the North Pacific High along the west coast of North America, the current extends all along the coast. A coastal, poleward undercurrent (the CUC) develops below the surface equatorward current, initially in the equatorward end of the model domain, and, during the upwelling season, along the entire coast.

As the wind turns equatorward and exerts stress on the water surface, Ekman transport offshore results in the upwelling of cooler water along the coast. (For example, see Fig. 8, which shows that the initial conditions of a horizontally uniform temperature field are changed by the presence of colder upwelled water near the coast). In spring the upwelling is confined to the south, while in summer it is present all along the coast.

As the core of the CUC intensifies, it shoals and displaces the core of the CC farther offshore (e.g. compare Fig. 7a and b). As Fig. 7a and b show, there are considerable vertical and horizontal shears in the upper layer currents. As a result, both types of instability (mixed) can exist simultaneously. Energy transfer calculations were performed for the time period (i.e. days 195–225) when the meanders and eddies developed. The results of the energy transfer analyses (not shown) show that both barotropic and baroclinic transfers are present in the coastal, equatorward region of the model domain. The transfers are strongest in the regions where meanders, filaments, and eddies subsequently develop.

The filaments that develop are "anchored" off of Cape Blanco, Cape Mendocino, and Point Arena (e.g. Fig. 8b and c). Note that the coldest, upwelling water is often found at or equatorward of large promontories (e.g. Cape Mendocino in Fig. 8c and d). Since promontories are areas of the irregular coastline where the alongshore component of the wind stress is at a local maximum, the CC, upwelling, and growth of filaments should be enhanced in these regions during the upwelling season (Batteen, 1997).

The equatorward CC also forms meanders in the vicinity of capes, which intensify and develop into predominantly cyclonic eddies. In time, these eddies coalesce with other cyclonic eddies to form relatively large ($\sim$ 100–300 km diameter) eddies. After the upwelling season, the equatorward CC takes the form of a meandering jet embedded with several cyclonic eddies (e.g. Fig. 8d).

3.2.2. Quasi-equilibrium phase

Using year 3 of the results of the longer experimental runs, we time-average the model output every 3 days for the months of January, April, July and October to see

the seasonal structure of features in the CCS. The results show that in spring (Fig. 9a) and summer (Fig. 9b), and throughout the upwelling season (Fig. 10a), there is a coastal, equatorward flow with speeds of $\sim$30–80 cm/s that leaves the coast between $\sim 42^{\circ}$N and 43°N, in the vicinity of Cape Blanco, and meanders downstream. The current then takes the form of a meandering jet. The jet has alongshore wavelengths of several hundred kilometers and cross-shore excursions of several

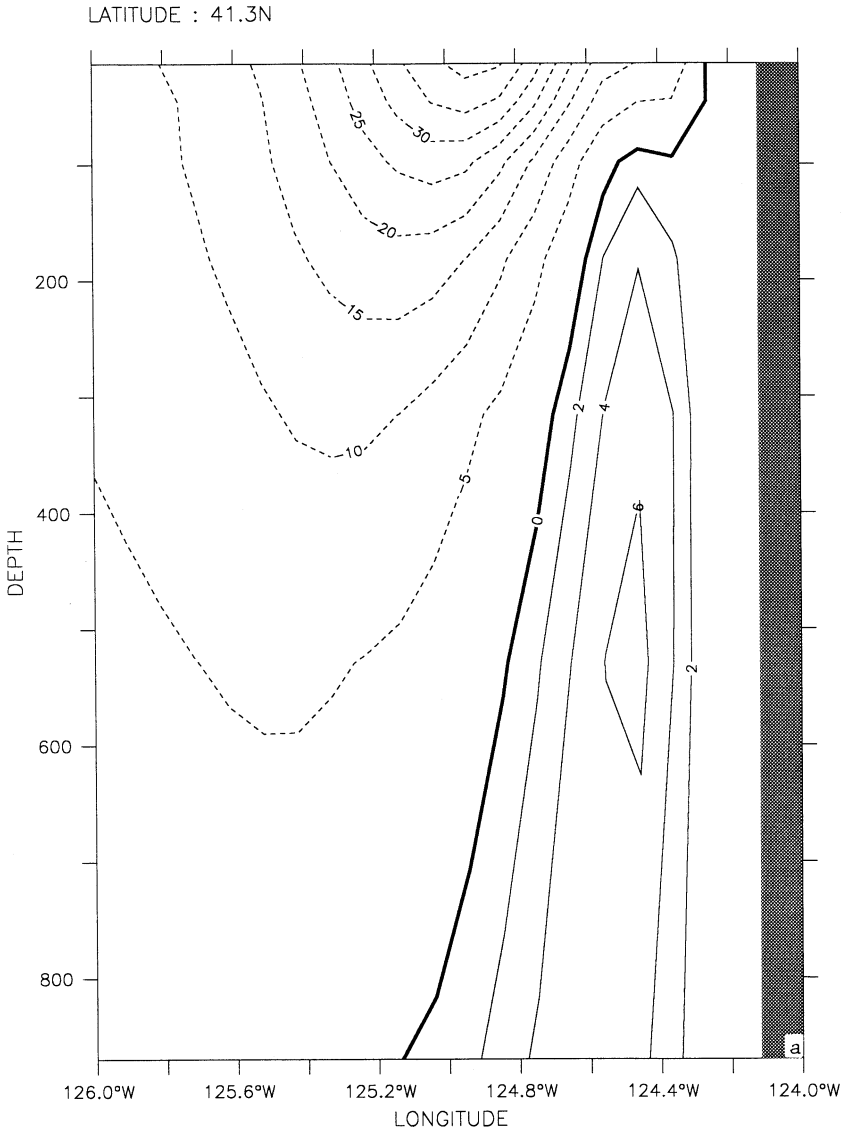

Fig. 7. Cross-shore section of meridional velocity (v) at 41.3N in the coastal region for Experiment 2 at days (a) 180 and (b) 195. The contour interval is 2 cm/s (5 cm/s) for poleward (equatorward) flow.

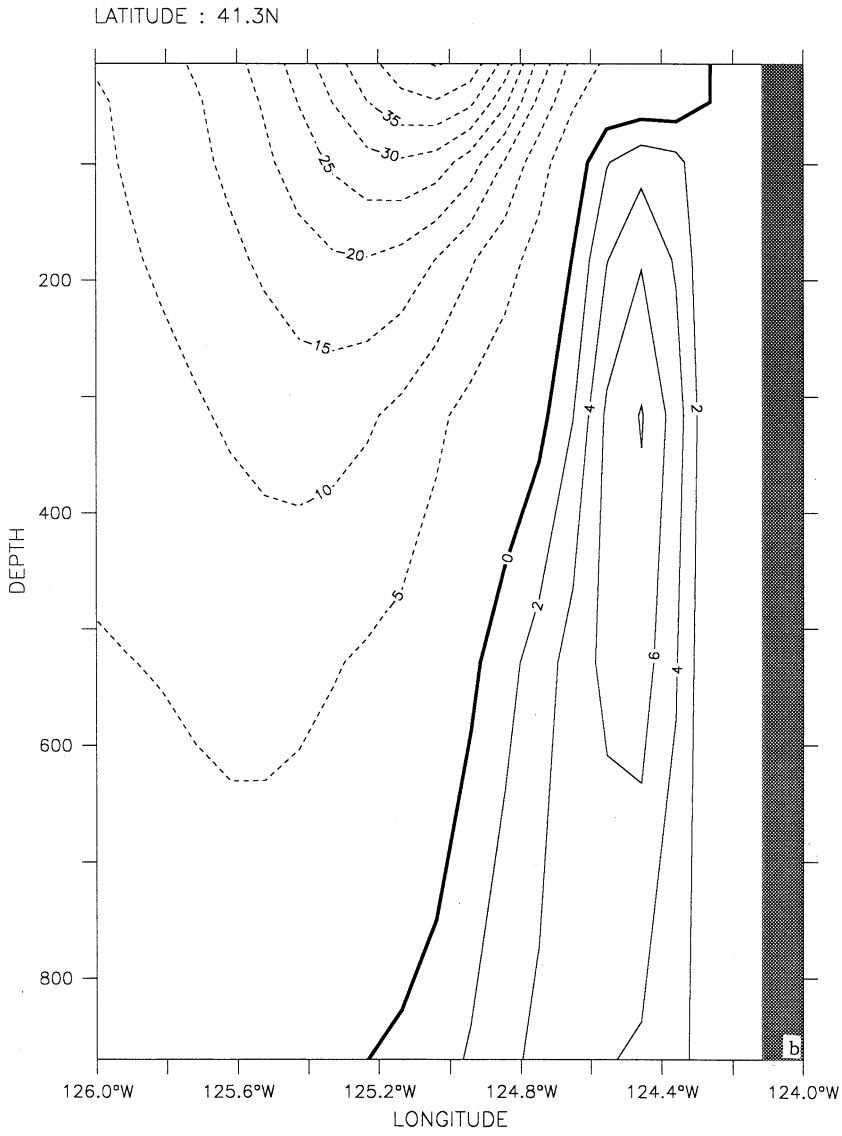

Fig. 7. Continued.

hundred kilometers, and it can extend to depths of $\sim$ 700 m (e.g. Fig. 10b). South of $\sim 43^{\circ}$N, inshore of the jet, there are both cyclonic and anticyclonic eddies. The cyclonic eddies tend to form in the vicinity of the capes. A comparison of the spring (Fig. 9a) and summer (Fig. 9b) velocity and temperature fields shows that as the eddies move westward, they can become embedded in the meandering jet. The results of the lower layer velocity fields, averaged over the upwelling season (Fig. 10c) show a coastal poleward undercurrent, with speeds of $\sim$ 10–20 cm/s, within $\sim$ 100 km of the coast.

After the upwelling season, i.e. in fall (e.g. Fig. 9c), a poleward flow, with speeds of $\sim$ 10–20 cm/s, develops within $\sim$ 100 km of the coast and subsequently replaces the coastal, equatorward flow. Offshore of the poleward flow are several cyclonic eddies. Farther offshore, there is a relatively strong ($\sim$ 50 cm/s) equatorward, meandering jet embedded with both cyclonic and anticyclonic eddies.

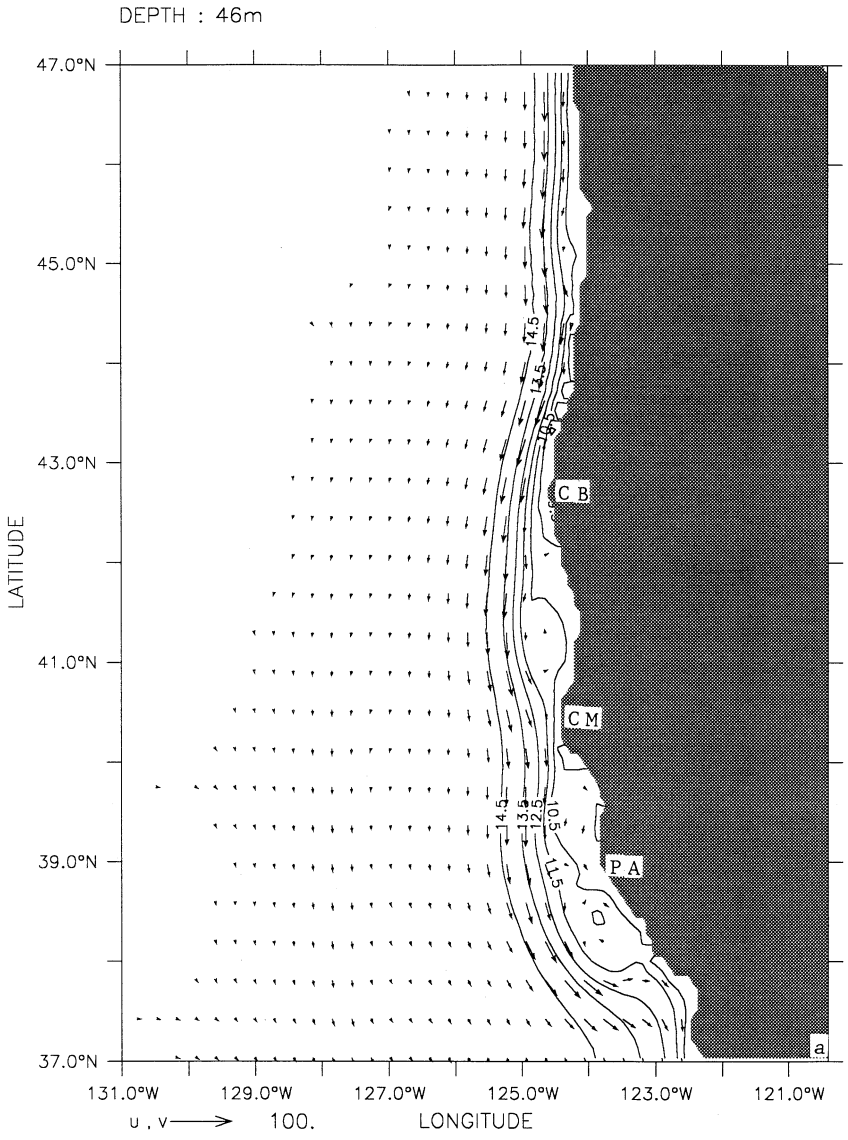

Fig. 8. Temperature contours and velocity vectors at 46 m depth for Experiment 2 at days (a) 225, (b) 255, (c) 270, and (d) 300. Contour interval is 1°C, maximum velocity vector is 100 cm/s.

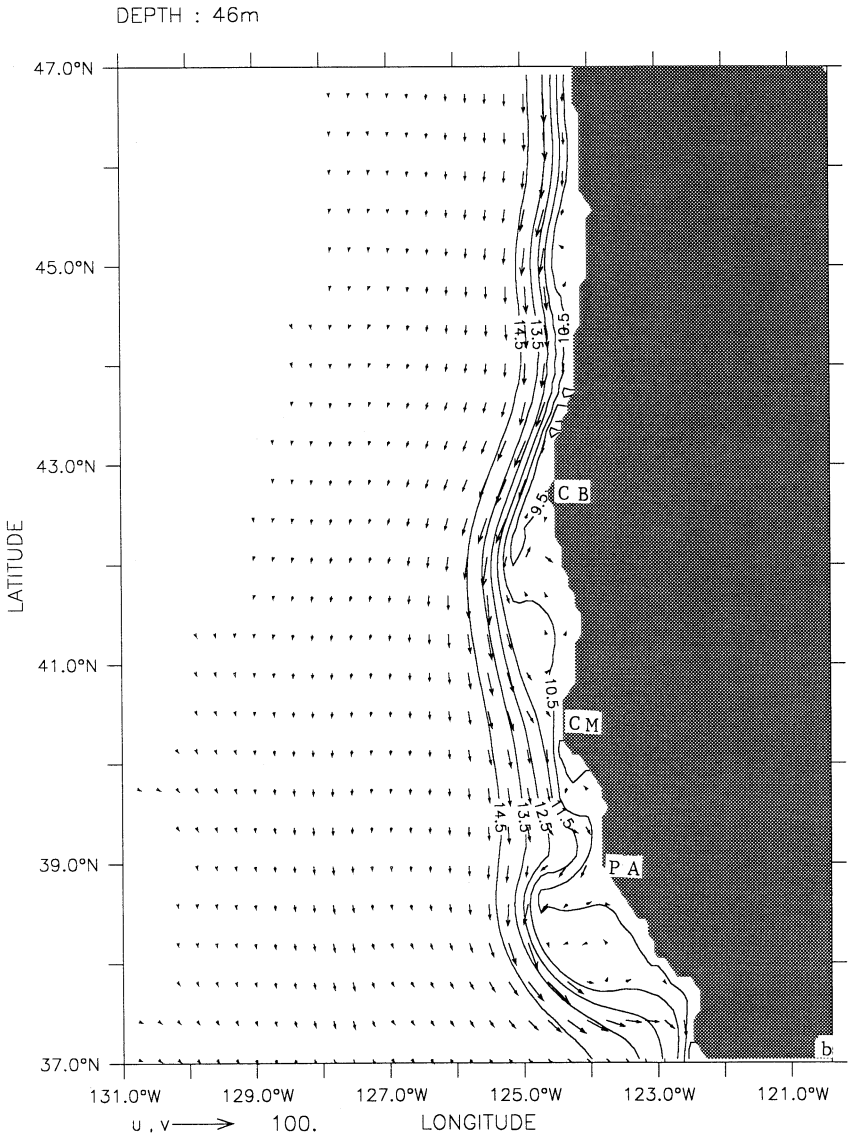

Fig. 8. Continued.

In the winter (e.g. Fig. 9d), in the poleward region of the model domain, the meandering jet is generally found farther offshore. In the equatorward part of the model domain, the jet meanders closer to shore, i.e. from $\sim 128°$W at 41°N to $\sim 125°$W at 38°N. Offshore and inshore of the jet, both cyclonic and anticyclonic eddies fill much of the model domain. A relatively strong surface poleward flow near the coast is still present north of $\sim 41°$N.

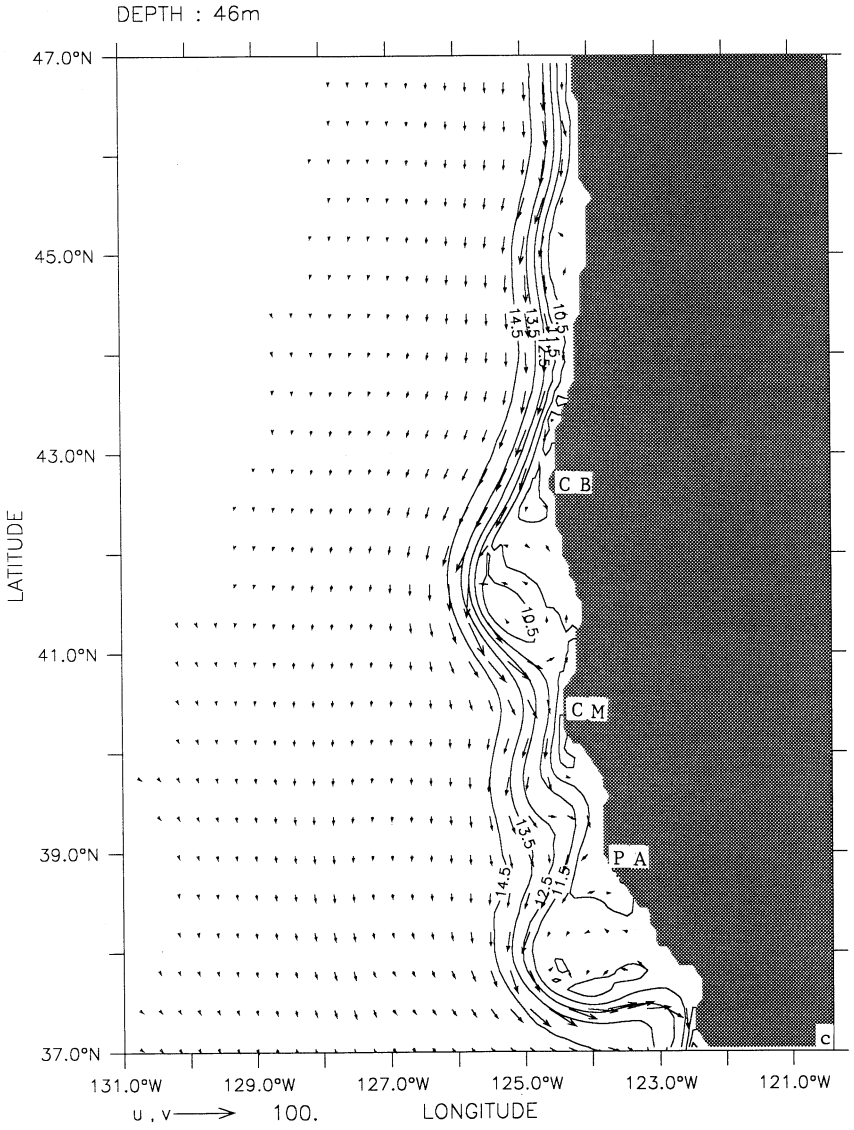

Fig. 8. Continued.

3.3. Experiment 3—seasonal wind forcing and thermohaline gradients

3.3.1. Spin-up phase

Due to the combination of thermohaline gradients and wind forcing, different oceanic responses are expected depending on the season. In the winter, in the poleward end of the model domain, the large high-to-low pressure gradient due to the

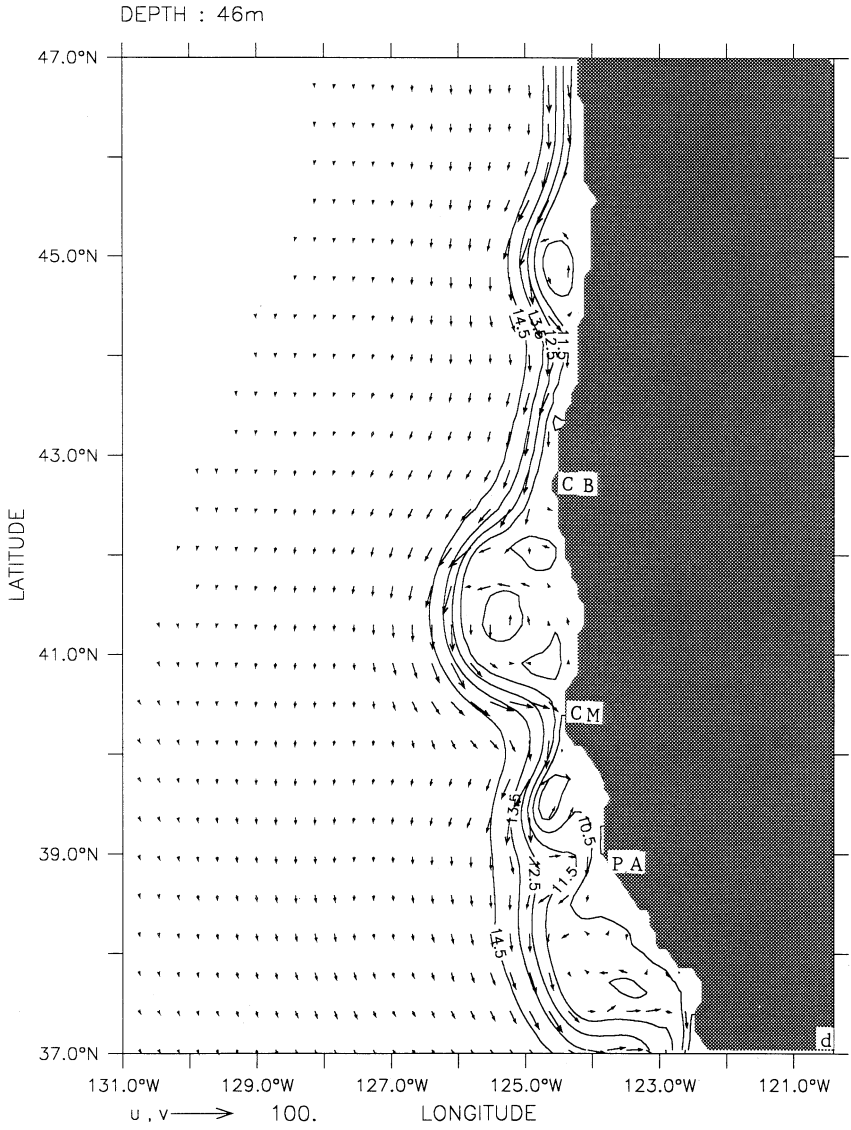

Fig. 8. Continued.

warm-to-cold temperature gradient establishes an onshore geostrophic flow, while the poleward wind stress results in onshore Ekman flow. On approaching the eastern boundary, the onshore flow turns and forms a poleward boundary current (e.g. Fig. 11a). In the equatorial end of the model domain, the smaller pressure gradient and the equatorward wind stress result in weak onshore geostrophic flow, offshore Ekman flow, and a coastal equatorward surface current (e.g. Fig. 11a).

During the upwelling season (~ April to September) (e.g. Fig. 11b–d), the combination of a weakened pressure gradient and increased equatorward winds over the entire model domain lead to a strengthening of equatorward flow all along the coast and a weakening (strengthening) of onshore (offshore) flow. As in Experiment 2, the upwelling is relatively uniform but has the coldest water found near coastal

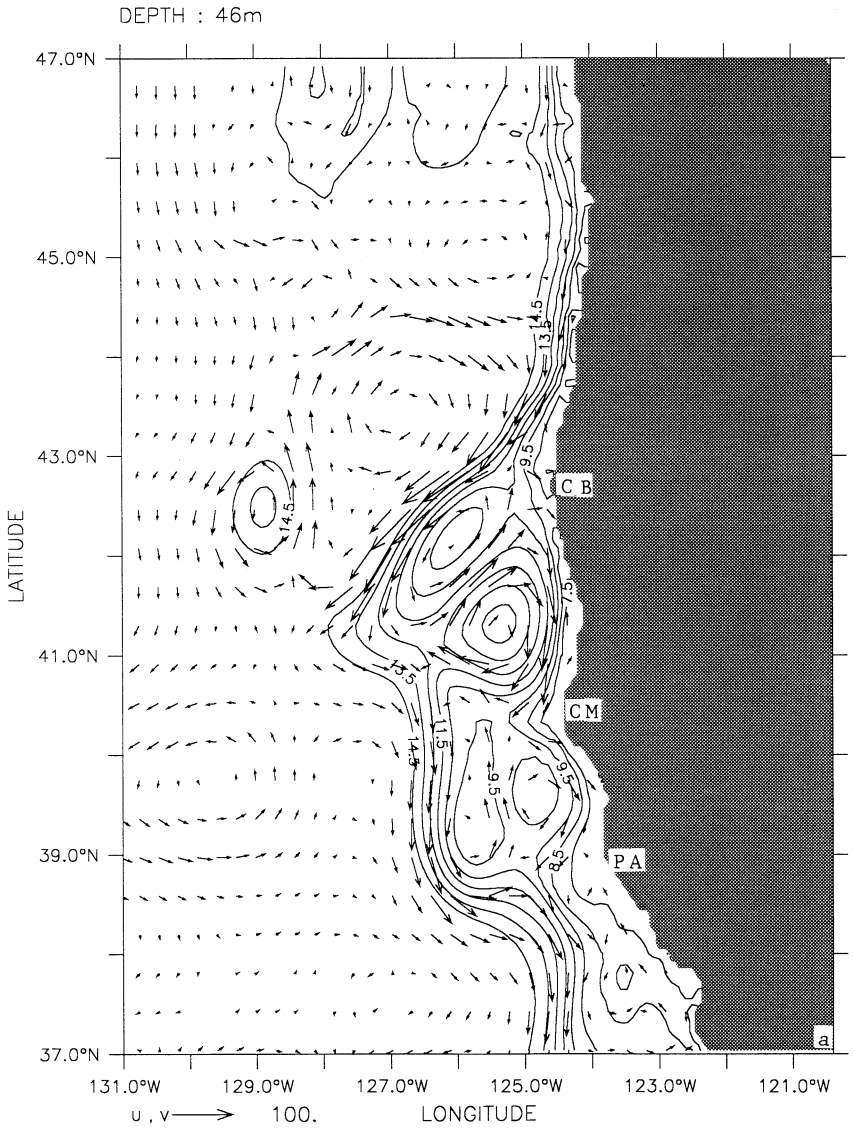

Fig. 9. Temperature and velocity vectors at 46 m depth for Experiment 2 in the third year of model simulation, time-averaged over the months of (a) April, (b) July, (c) October, and (d) December. Contour interval is 1°C; maximum velocity vector is 100 cm/s.

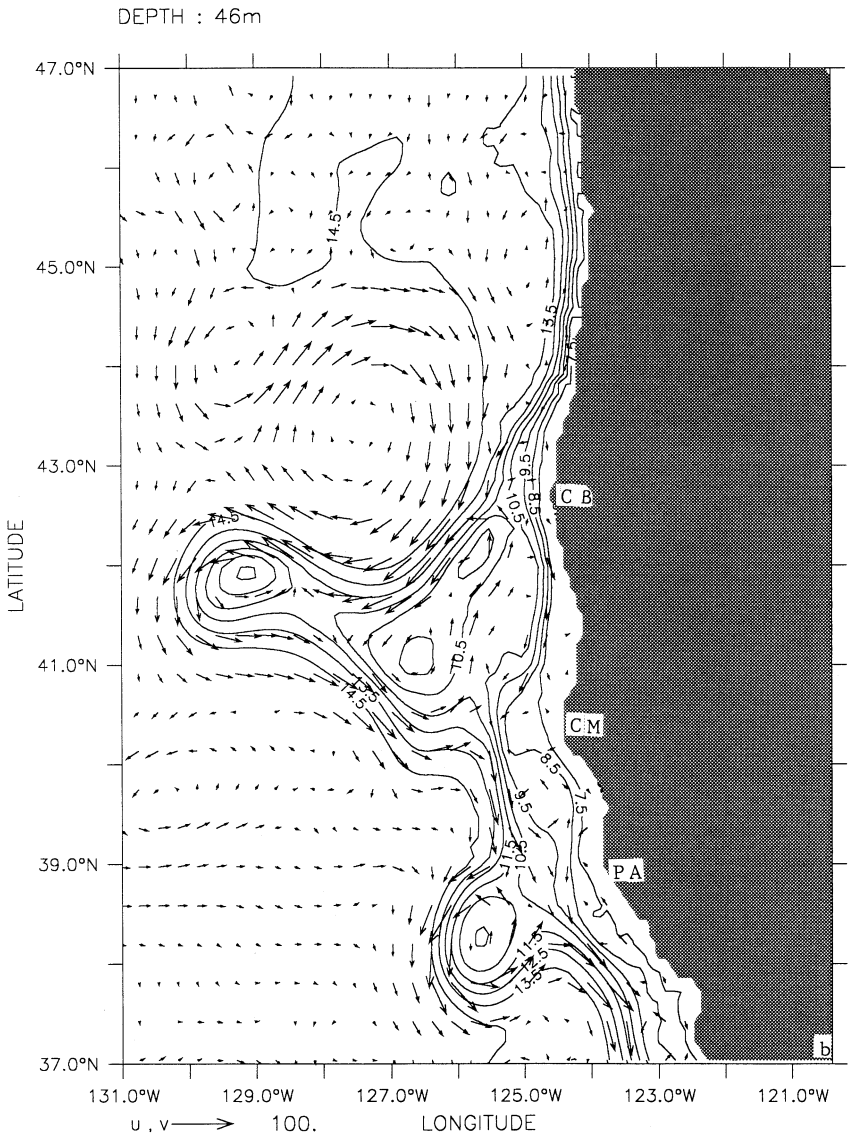

Fig. 9. Continued.

promontories (e.g. Cape Blanco in Fig. 11d). The subsurface structure of the currents shows that there is a poleward undercurrent (e.g. Fig. 12a). The undercurrent is within $\sim$ 150 km of the coast, extends from $\sim$ 150 to greater than 700 m depth, and has a core velocity of $\sim$ 5 cm/s. Typical core velocities for the undercurrent range from $\sim$ 5 to 20 cm/s. The surface coastal equatorward flow extends to $\sim$ 150 m depth-near shore to $\sim$ 500 m depth offshore. The core of the surface current is within $\sim$ 100 km

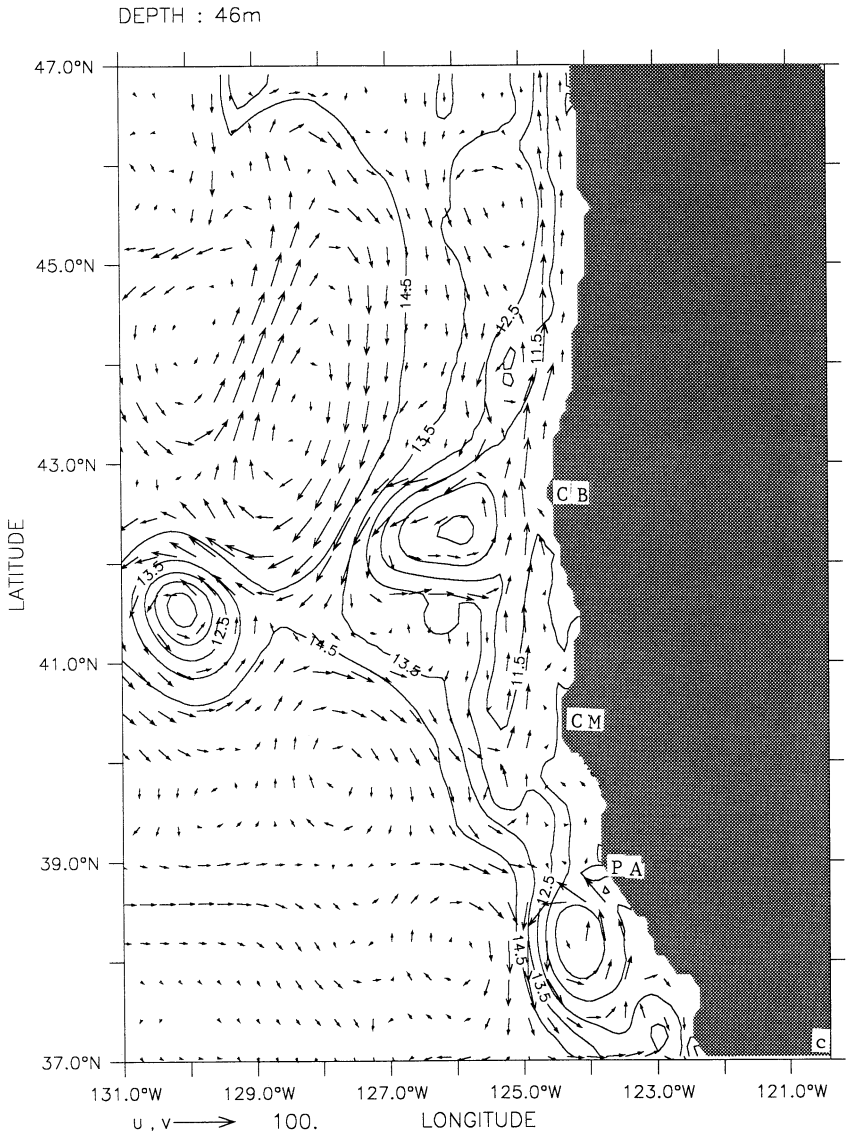

Fig. 9. Continued.

of the coast and has a typical core velocity of $\sim$ 50–70 cm/s. The upwelling season model simulations are consistent with observed depths and velocities of both the surface equatorward current and the poleward undercurrent (e.g. Huyer et al., 1991).

In the fall, as expected, the surface poleward flow strengthens in the coastal poleward end of the model domain in response to both the strengthening of the pressure gradient and the return of poleward wind stress in the region. The subsurface

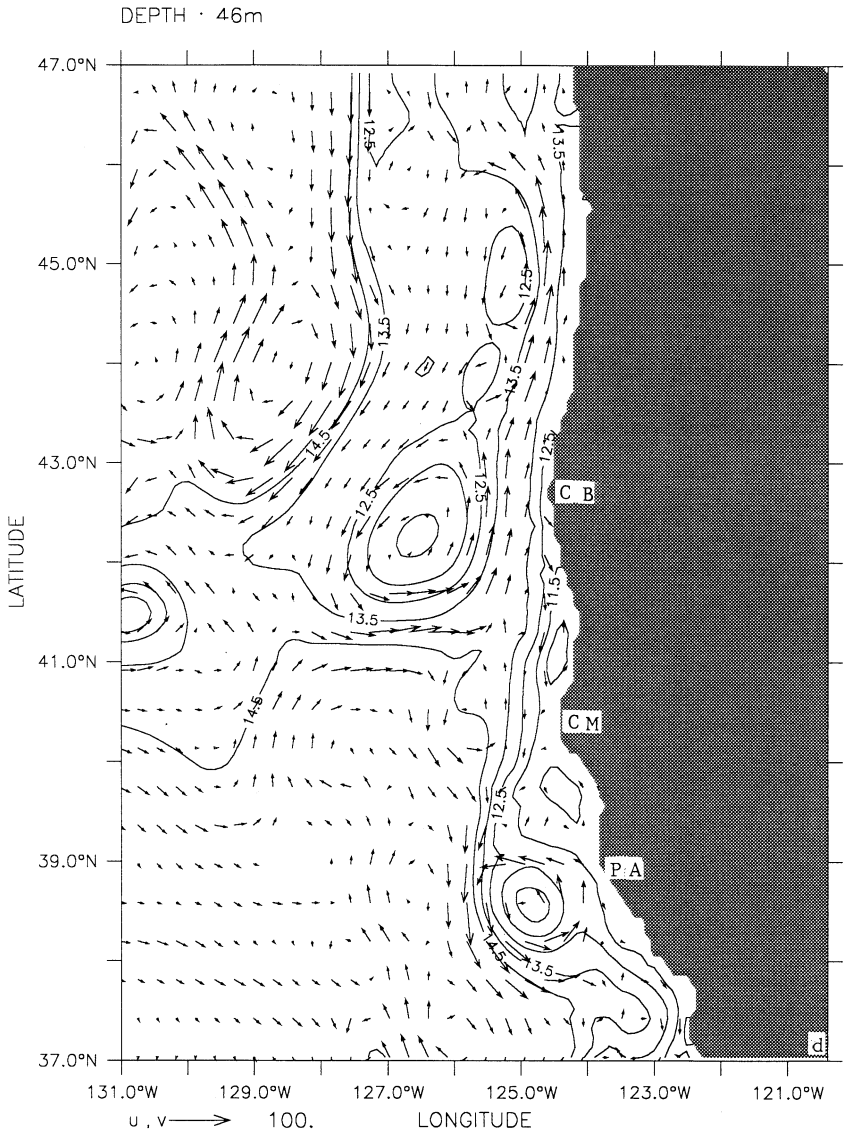

Fig. 9. Continued.

structure of the currents shows that in the poleward end of the model domain, there is an equatorward undercurrent (e.g. Fig. 12b). The undercurrent is within $\sim$ 30 km of the coast, extends from $\sim$ 150–700 m depth, and has a core velocity of $\sim$ 2 cm/s. Typical velocities for the undercurrent range from $\sim$ 2 to 5 cm/s. As in Experiment 1, the fall model simulation in the poleward end of the model domain is consistent with the observed depths and velocities of both the surface poleward current and the equatorward undercurrent near the coast of Washington (Hickey, 1979, 1998).

3.3.2. Quasi-equilibrium phase

Longer run times (~ 3 years) of the model simulation show that during the upwelling season many of the features simulated in Experiment 2, such as meanders, eddies, a temperature front, and filaments (e.g. Fig. 9 and 10), are also, as expected

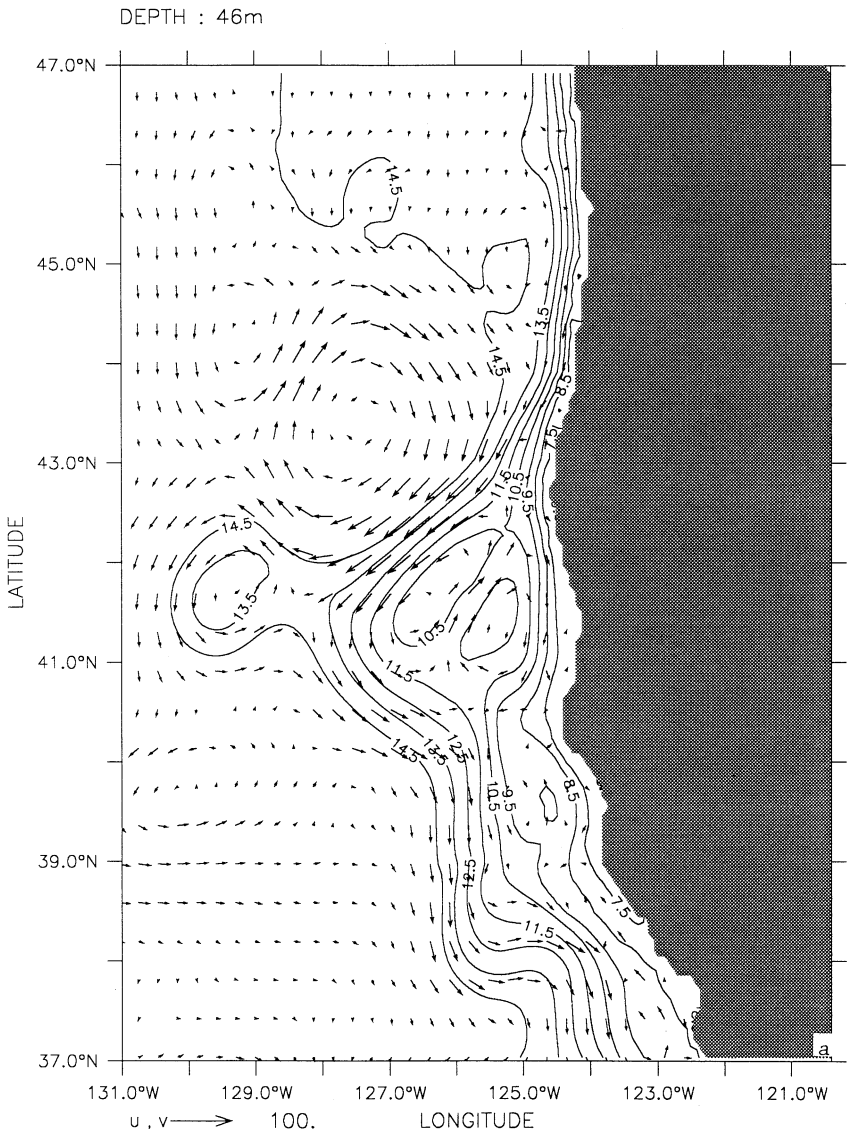

Fig. 10. Time-averaged (over the months of April–September of year 3) plots for the upwelling season for Experiment 2 of (a) temperature contours and velocity vectors at 46 m depth, (b) cross-section of at 41.3N, and (c) velocity vectors at 316 m depth. Contour interval is 1°C in (a) and 5 cm/s in (b). Maximum velocity vector is 100 cm/s in (a) and (c).

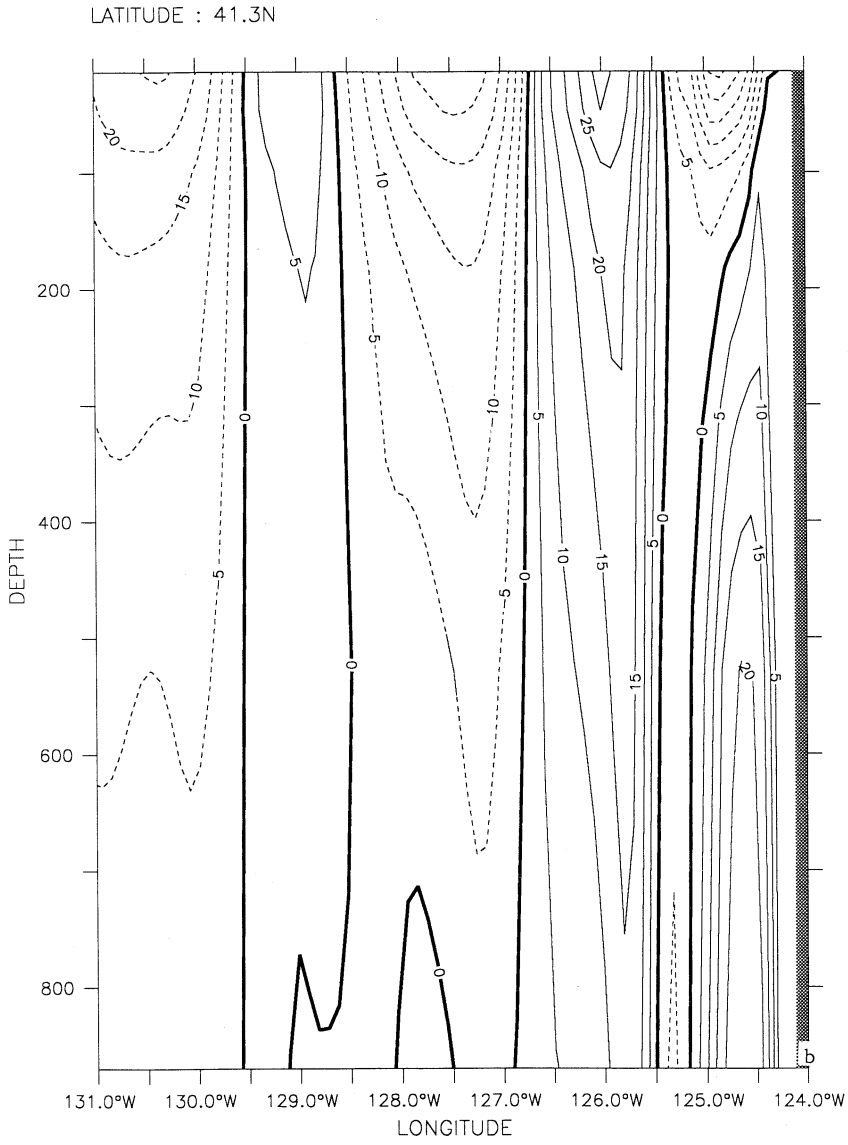

Fig. 10. Continued.

with the dominance of wind forcing, simulated in Experiment 3. A comparison of these features for Experiments 2 and 3 during the upwelling season (Fig. 10a and 13, respectively) shows that the results are qualitatively similar except that there is a tighter temperature gradient inshore of $\sim 125^{\circ}$W between Cape Mendocino and Point Arena in Experiment 3. This must be due to the onshore geostrophic flow resulting from the alongshore pressure gradient.

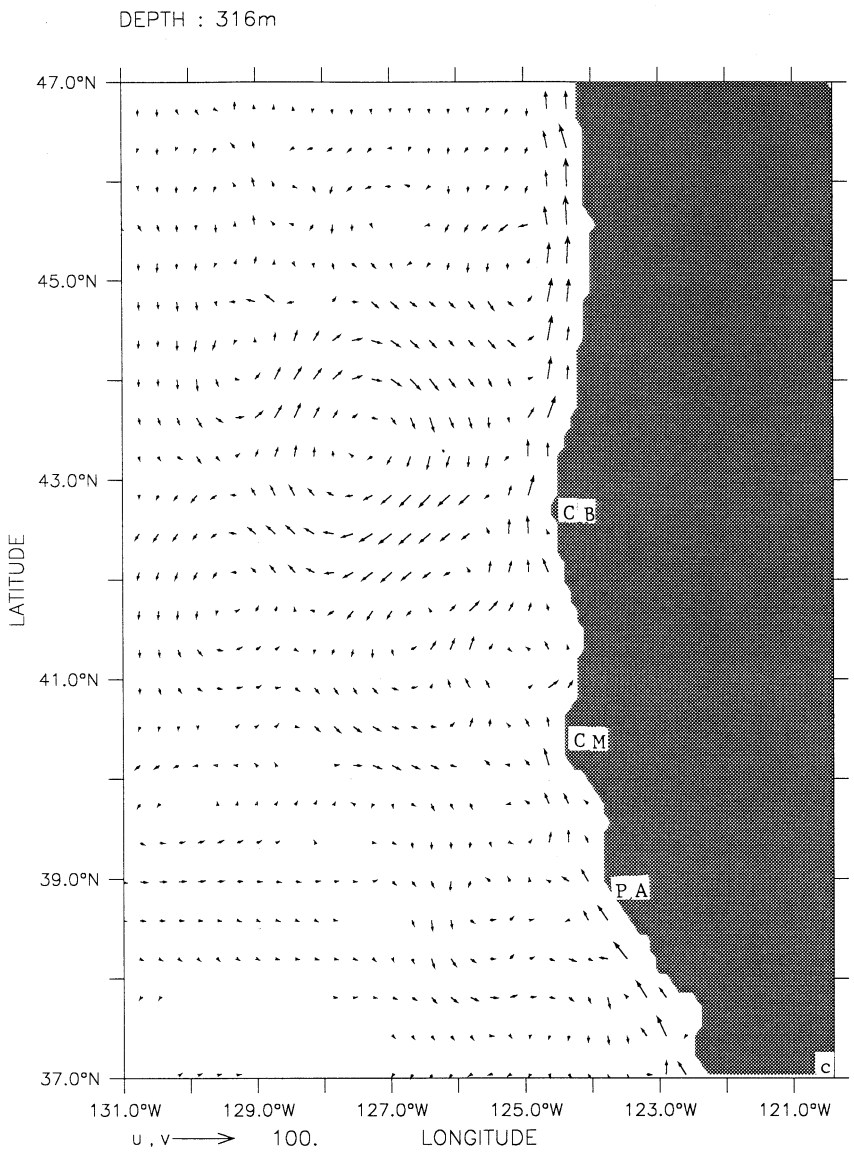

Fig. 10. Continued.

Stronger surface and subsurface currents inshore of $\sim 125°$W in Experiment 3 also are found between Cape Mendocino and Point Arena. For example, Figs. 14a and b show that the surface coastal jet with velocities of ~ 10 cm/s north of Cape Mendocino (Fig. 14a) intensifies to ~ 50 cm/s at Cape Mendocino (Fig. 14b), while the undercurrent with velocities of ~ 15 cm/s north of Cape Mendocino intensifies to ~ 25 cm/s at Cape Mendocino.

In the poleward end of the model domain, a comparison of subsurface currents (not shown) for Experiments 2 and 3 shows that the velocities for the undercurrent decrease from ~ 45 cm/s in Experiment 2 to ~ 20 cm/s in Experiment 3. The reduction in the velocities for the poleward undercurrent is likely due to the net result

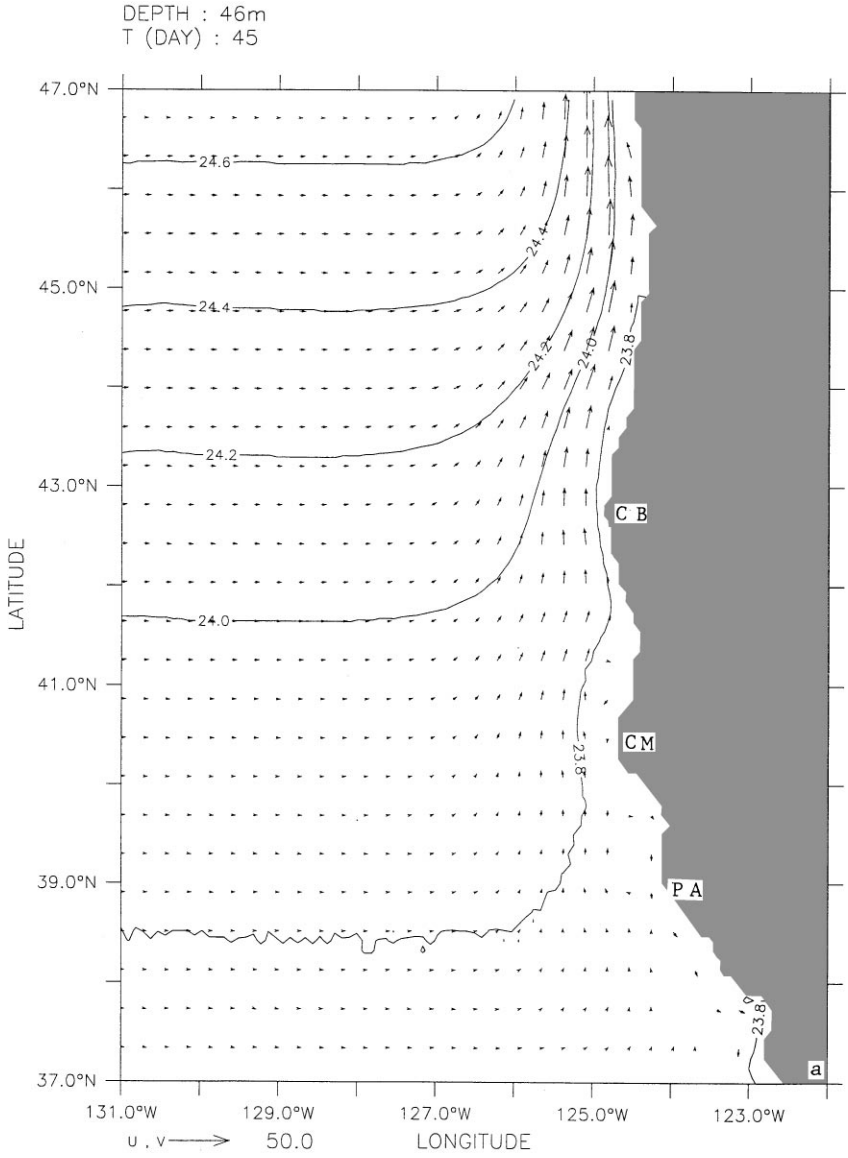

Fig. 11. Density contours and velocity vectors at 46 m depth for Experiment 3 at days (a) 45, (b) 87, (c) 180, and (d) 255. Contour interval is 0.2 gm/cm^3; maximum velocity vector is 50 cm/s.

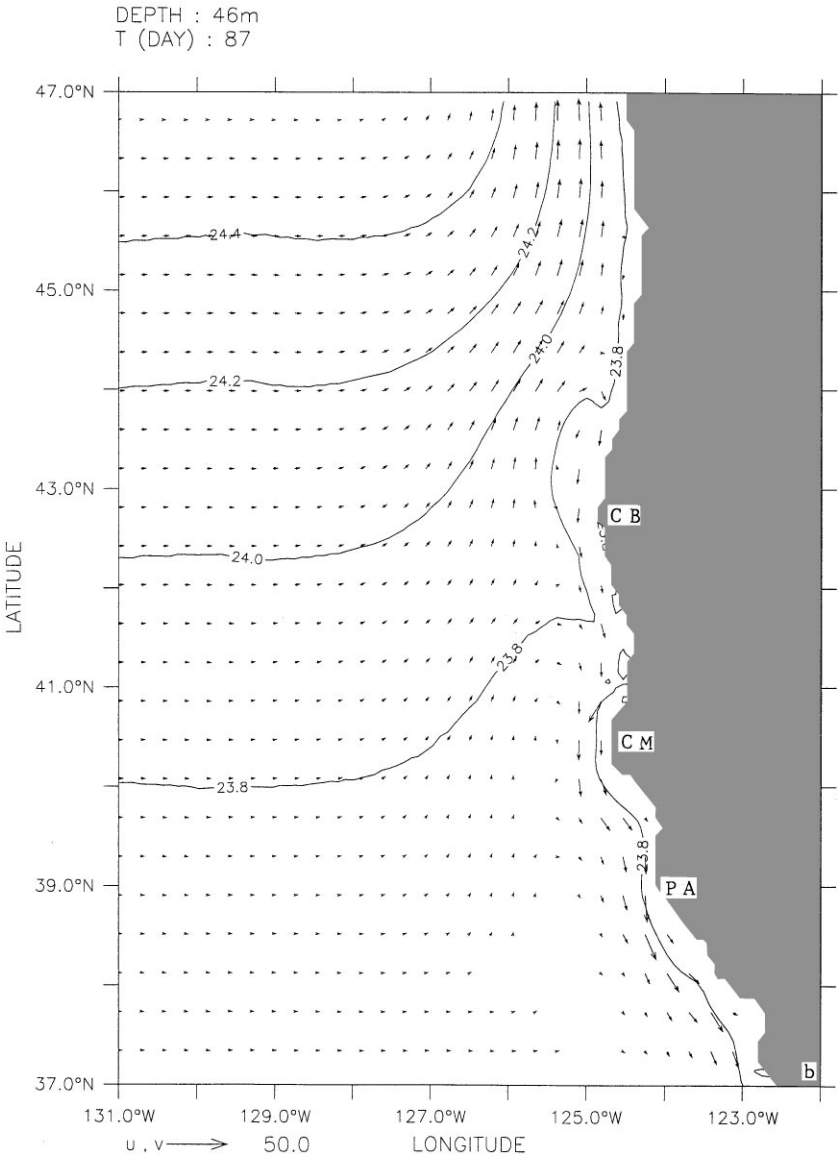

Fig. 11. Continued.

of a poleward undercurrent generated by wind forcing opposing an equatorward undercurrent generated by thermohaline forcing in this region.

Horizontal maps of the upper layer mean kinetic energy (MKE) and eddy kinetic energy (EKE), averaged over the duration of the upwelling season (Fig. 15a and b) are suggestive of where the mean and eddy energy sources are to be found (Holland et al.,

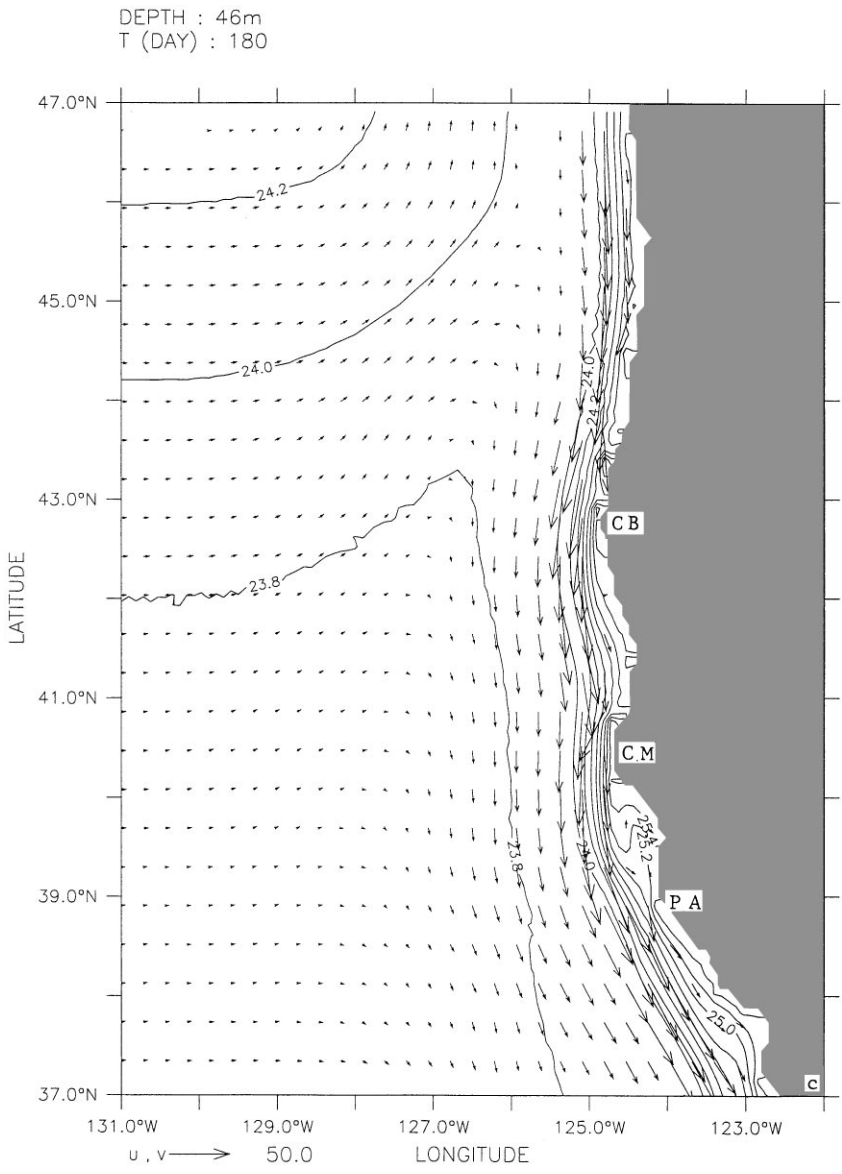

Fig. 11. Continued.

1983). A comparison of Figs. 13 and 15 shows that high values of MKE and EKE are found all along the coastal and offshore axes of the equatorward jet, and in the offshore regions south of $\sim 42°$N.

A comparison of Figs 15a and b shows that maximum values of MKE and EKE occur in the same region, i.e. inshore of $\sim 125°$W between Cape Mendocino and

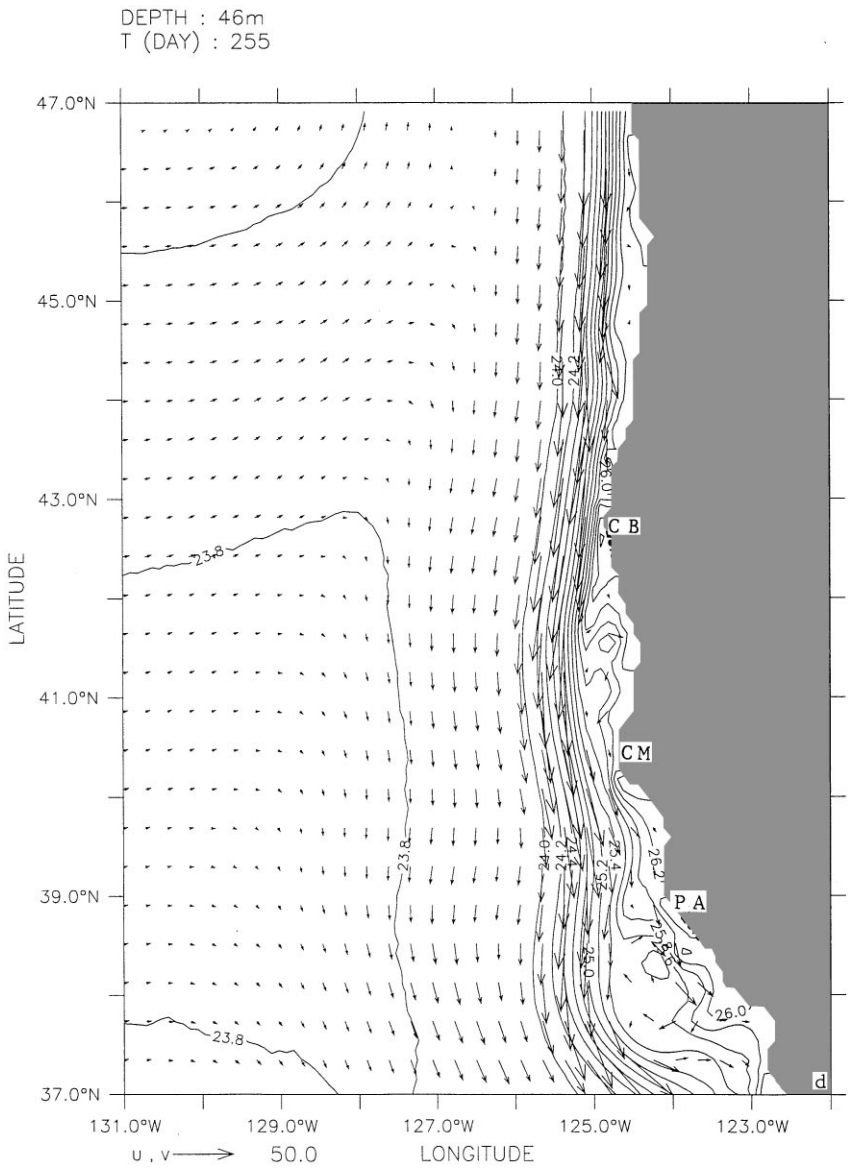

Fig. 11. Continued.

Point Arena. Note that the MKE values are larger than the EKE values in the region. This is consistent with the results of Batteen (1997), which showed that the eddies are generated from instabilities of the mean equatorward current and the poleward undercurrent via baroclinic and/or barotropic instability processes.

Maps of EKE for each month during the upwelling season (not shown) show that the maximum EKE always occurs between ~37 to 39°N and between 124 and 128°W. The maps also show that high values of EKE are present throughout the upwelling season between Cape Mendocino and Point Arena, while off of Cape Blanco, EKE values steadily increase from small to large values as the upwelling

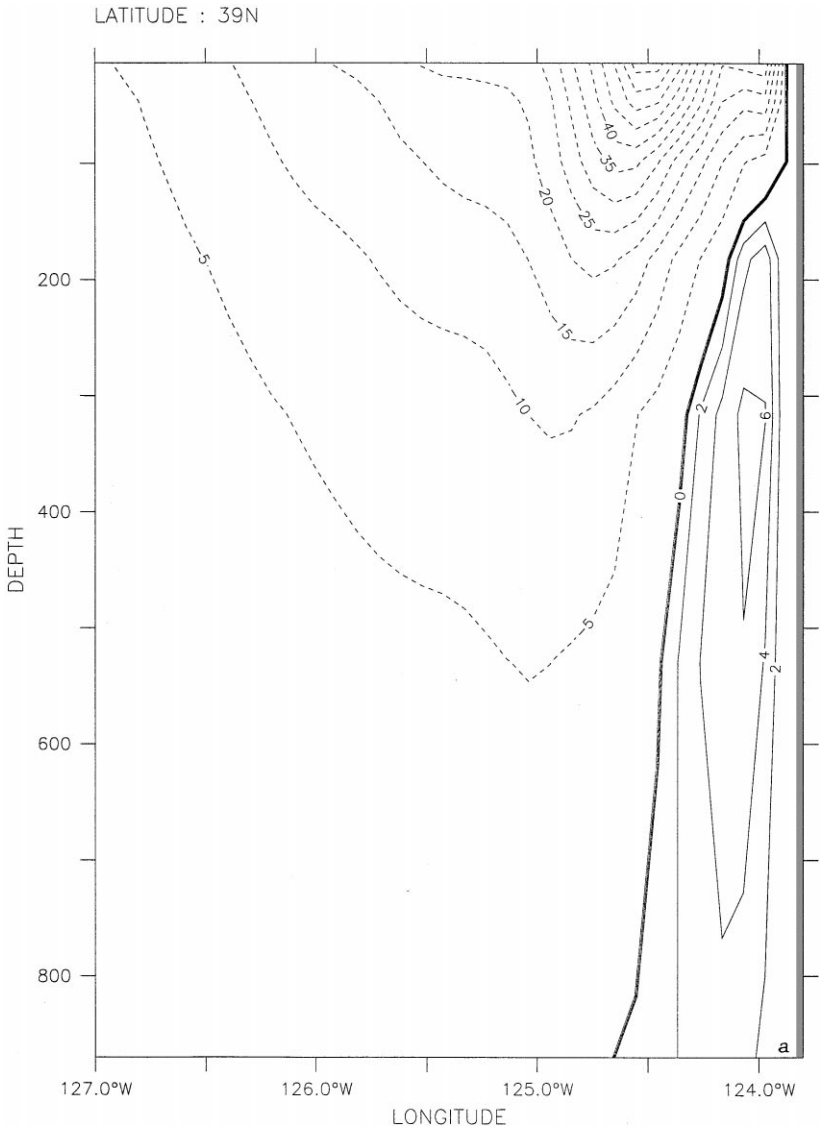

Fig. 12. Cross-shore section of meridional velocity (v) in the coastal region for Experiment 3 for days (a) 180 at 39N, and (b) 300 at 46N. For equatorward flow, contour interval is 1 cm/s for values less than 5 cm/s and 5 cm/s for values greater than 5 cm/s. For poleward flow, contour interval is 2 cm/s in (a) and 5 cm/s in (b).

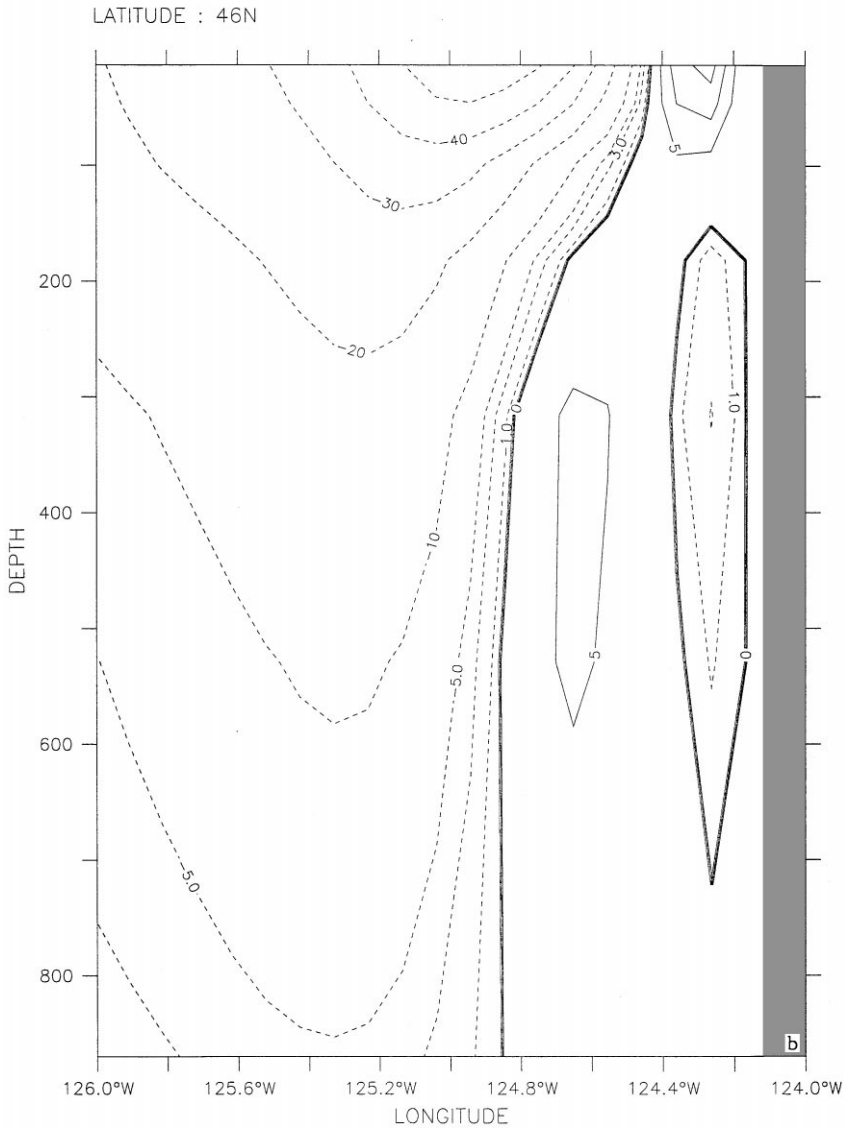

Fig. 12. Continued.

season progresses, with highest values occurring in July and August. These results suggest that the greatest eddy activity off of Cape Blanco occurs after June, while eddy activity between Cape Mendocino and Point Arena occurs regularly throughout the upwelling season.

After the upwelling season, i.e. in the fall, the combination of wind forcing and thermohaline gradients results in the seasonal changes in the currents in the poleward

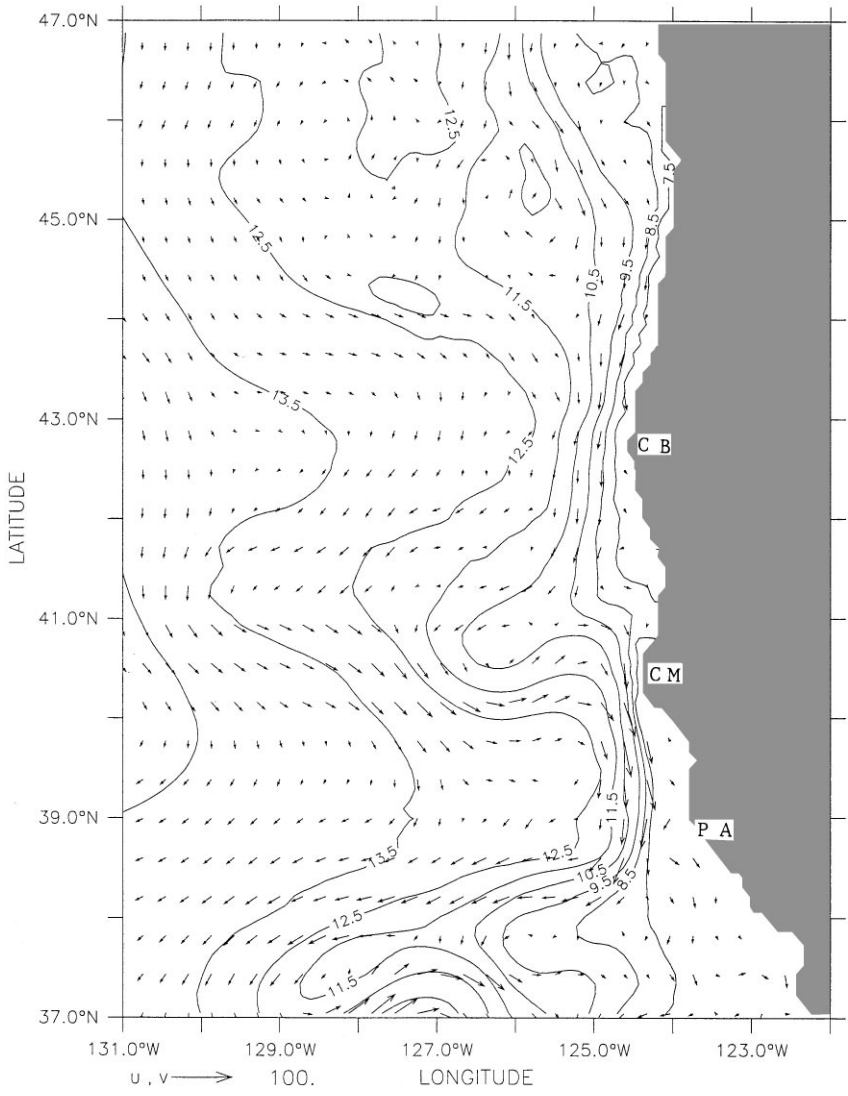

Fig. 13. Temperature contours and velocity vectors at 46 m depth for Experiment 3 in the third year of model simulation for days 90–270. Contour interval is 1°C; maximum velocity vector is 50 cm/s.

end of the model domain. In particular, the reversal of winds from equatorward to poleward combined with the intensification of the alongshore pressure gradient results in a shoaling of the poleward undercurrent near the coast of Oregon and Washington, as seen in the latitudinal sequence of Fig. 16a–c. These results are consistent with the hypothesis of Hickey (1979, 1998) that a surface poleward current can result from a shoaling of the undercurrent.

3.3.3. Comparison of model results with observations

Because these studies are not model hindcasts but are idealized process-oriented studies, we cannot make direct comparisons with data; however, we can investigate whether the phenomenological model behavior is qualitatively similar to observational data in the CCS. Since the effects of wind forcing dominate the effects of

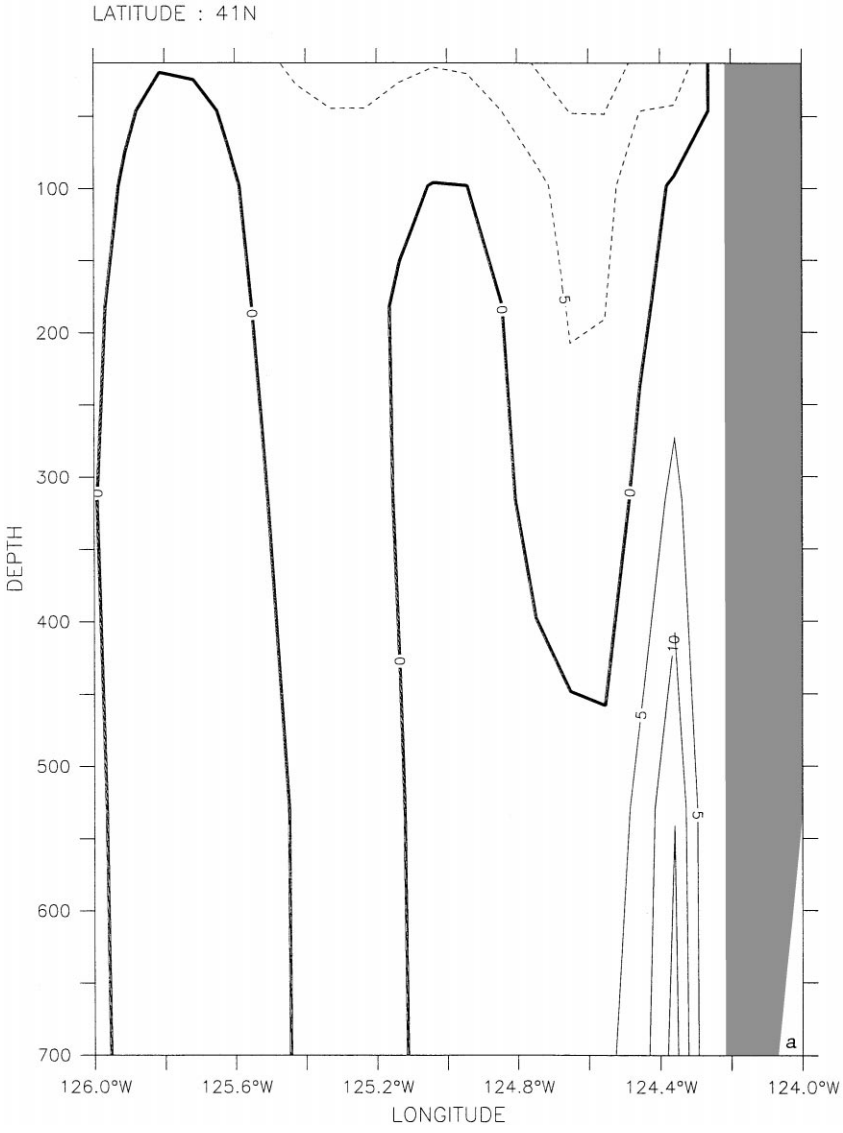

Fig. 14. Cross-shore sections of meridional velocity (v) for Experiment 3 in the third year of model simulation, time-averaged for days 90–270 at (a) 41N, and (b) 40.2N. Contour interval is 5 cm/s.

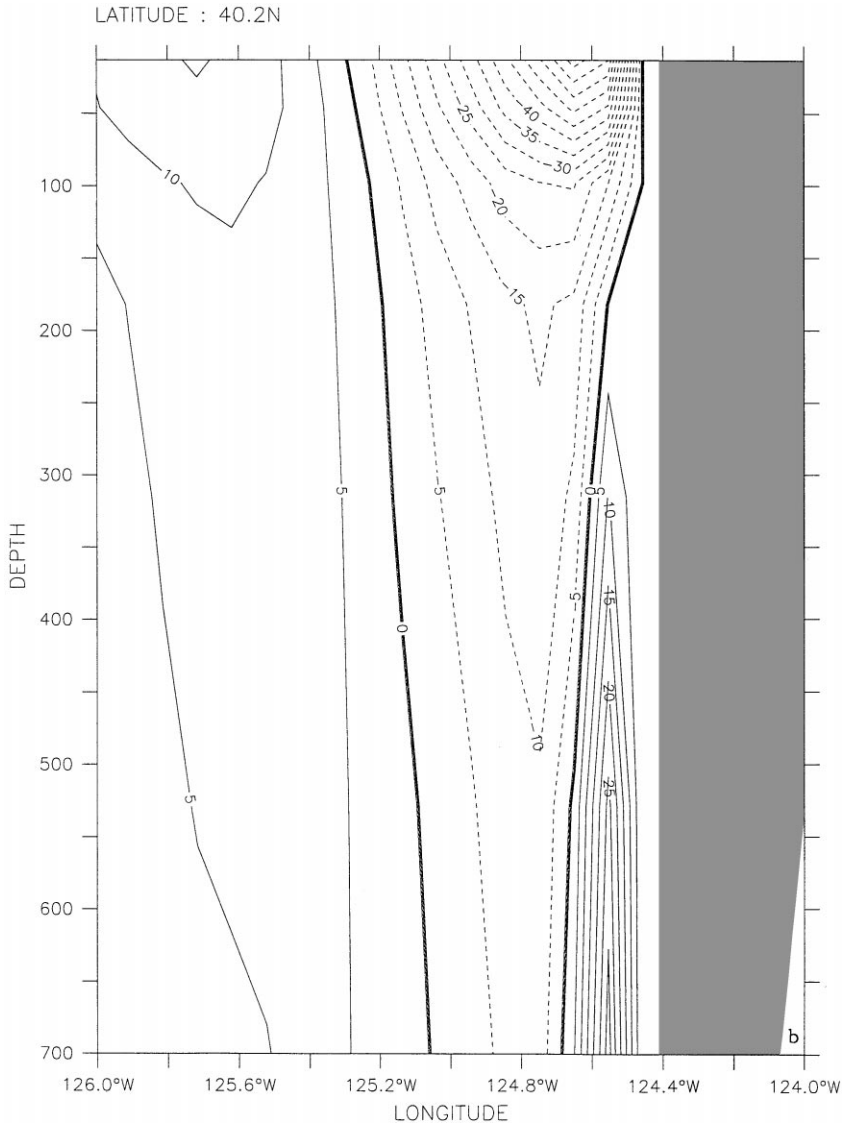

Fig. 14. Continued.

thermohaline gradients in the CCS, we will only use Experiments 2 and 3 in the comparisons. Overall, the results of Experiment 3's complex flow regime highlights the major characteristics of the CCS with relatively close similarities to field observations.

In both Experiments 2 and 3 the numerical model, consistent with observations, developed a coastal, equatorward surface flow and a coastal, poleward undercurrent

during the upwelling season, and a poleward, coastal surface flow in the poleward end of the model domain during the fall and winter. Only Experiment 3 produced a coastal, equatorward undercurrent during the fall and winter. Neither experiment produced the Davidson Current, which is thought to be generated near Point Conception (Hickey, 1979, 1998), which lies outside the model domain. The velocities,

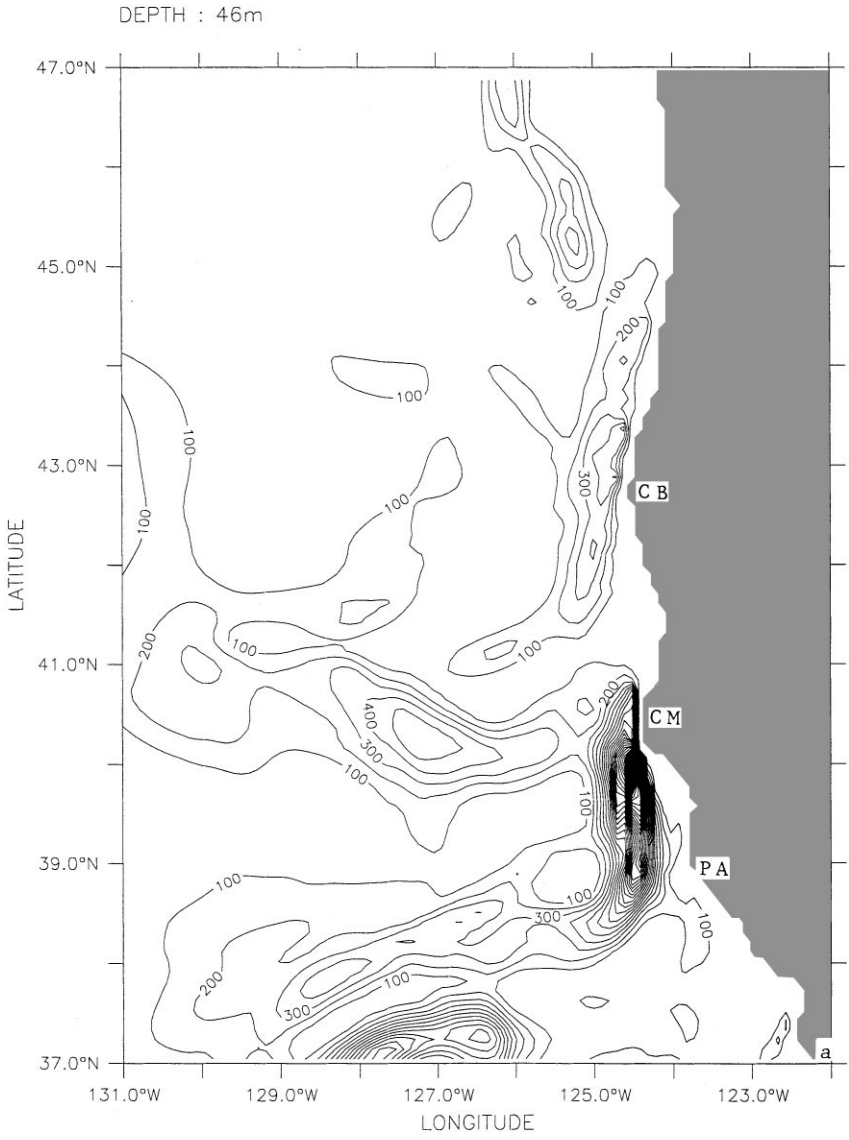

Fig. 15. Horizontal maps at 46 m depth of (a) mean kinetic energy (MKE), and (b) eddy kinetic energy (EKE) for Experiment 3 in the third year of model simulation, time-averaged for days 90–270. Contour interval is 100 cm^2/s^2.

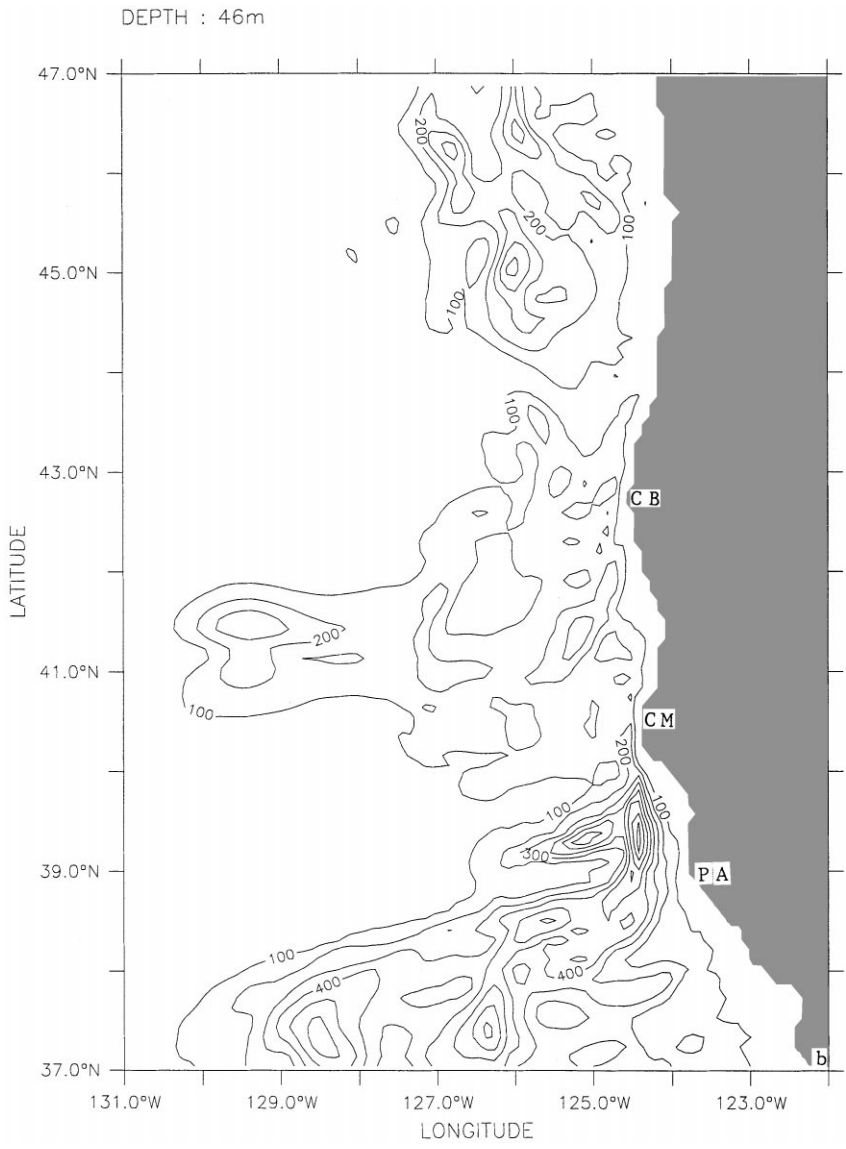

Fig. 15. Continued.

offshore locations and extents of the currents generated in both experiments compared favorably with observations, except for the velocity of the undercurrent in Experiment 2, which was more than double observed values (e.g. Huyer et al., 1991) in the poleward end of the model domain. The depth of the currents in both experiments also extended deeper than observed values, which may be due to the absence of shelf and slope topography.

Both experiments produced mesoscale meanders, eddies, and jet-like surface currents, which were superimposed on the large scale flow. Consistent with observations (e.g. Bernstein et al., 1977; Simpson et al., 1984), the eddies had wavelengths of the order of 100 km, time scales of months (e.g. see Fig. 9), could be anticyclonic or cyclonic, and could extend to at least 300 m depth (see Fig. 10b). The filaments generated in both experiments agreed well with observations (e.g. Brink and Cowles,

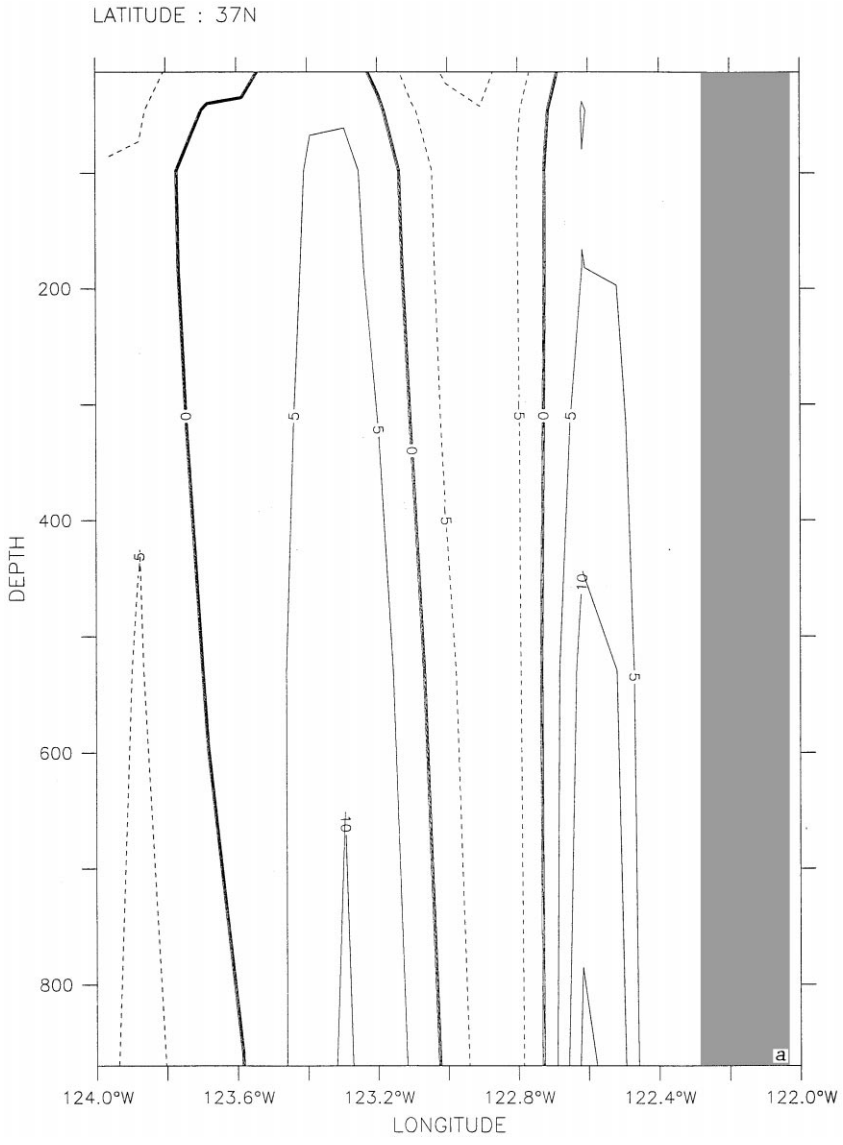

Fig. 16. Cross-shore sections of meridional velocity (v) for Experiment 3 in the third year of model simulation, time-averaged for days 270–363 at (a) 37N, (b) 43N, and (c) 46N. Contour interval is 5 cm/s.

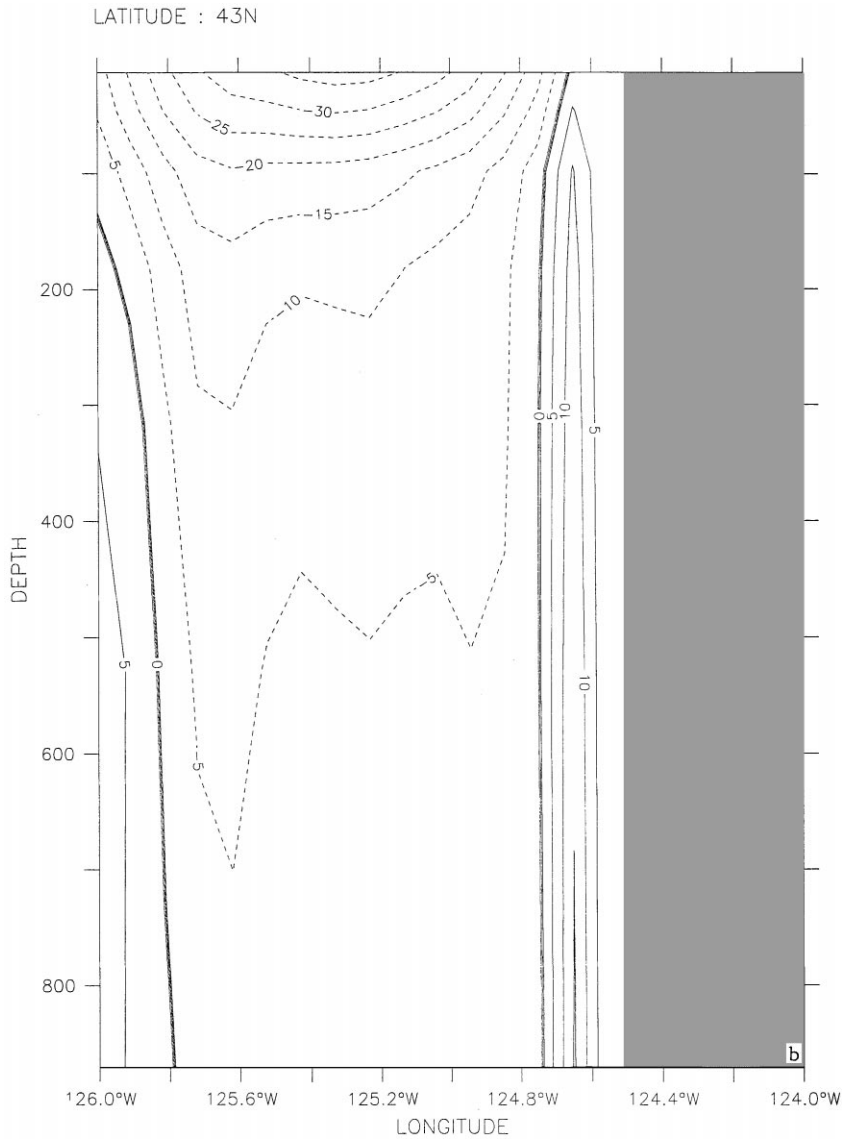

Fig. 16. Continued.

1991), which show that the filaments can exhibit a 1°–3°C temperature change across their boundaries, and can extend to at least ~100–200 m depth, with a width of ~20–100 km at the surface, and with peak speeds of ~50–100 cm/s. Both experiments also showed that the equatorward current could take the form of a meandering jet, with wavelengths of ~100–300 km, consistent with satellite observations (e.g. Bernstein et al., 1977).

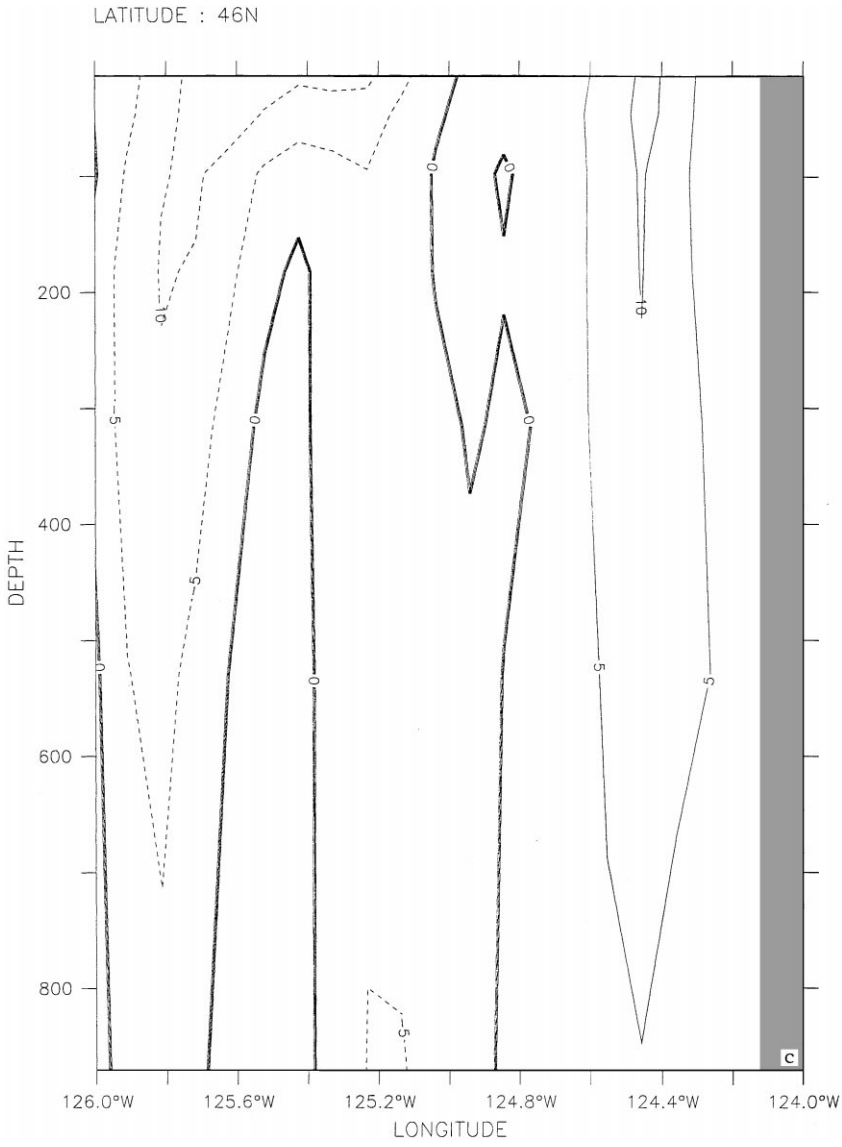

Fig. 16. Continued.

Both Strub and James (1995) (hereafter referred to as SJ95) and our results show that there is a connection between the equatorward flow off Oregon and the jet that meanders along a temperature front off California, i.e. the equatorward flow off Oregon and the meandering jet are part of a continuous flow that originates from farther north. In particular both SJ95 (see Fig. 2a of SJ95) and our results (Fig. 10 and 13) show the presence of a coastal equatorward flow leaving the coast in the vicinity of

Cape Blanco. Downstream from Cape Blanco, both SJ95 and our results show the equatorward jet meandering offshore and then nearshore in the vicinity of Cape Mendocino. While SJ95 and the results of Experiment 3 show that the jet and its associated temperature front between Cape Mendocino and Point Arena are formed inshore of $\sim 125°$W, the results of Experiment 2 show that these features extend farther offshore to $\sim 126°$W. South of Cape Mendocino, SJ95 and the results of Experiment 3 show the jet veering offshore, while the results of Experiment 2 show the jet veering inshore.

The EKE results of our model simulations from Experiment 3 compare well with near-surface EKE measurements obtained from altimetric, drifter, and moored current meter observations in the CCS by Kelly et al. (1998). While Kelly et al. (1998) and the results of both experiments show the location of maximum EKE to be between $\sim 36°$N and 40°N during the upwelling season, Kelly et al. (1998) and the results of Experiment 3 (see Fig. 15b) show the longitudinal location to be at $\sim 125°$W rather than at $\sim 126°$W as shown by Experiment 2 (not shown). This region of maximum EKE also is shown to coincide with increased equatorward flow in both Kelly et al. (1998) and in the results of both experiments. While the EKE results of Experiment 2 (not shown) show that south of $\sim 40°$N, on a seasonal time scale, the region of monthly maximum EKE migrates westward to $\sim 126°$W, both Kelly et al. (1998) and the results of Experiment 3 (not shown) show that the region of monthly maximum EKE migrates westward to $\sim 128°$W.

On the basis of these results we can conclude that even though the effects of wind forcing dominate the CCS, the additional effects of the thermohaline gradients result in the following: the development of a poleward surface current and an equatorward undercurrent in the poleward end of the model region; an onshore geostrophic component, which results in a temperature front and stronger surface and subsurface currents between Cape Mendocino and Point Arena; and a region of maximum EKE inshore of $\sim 125°$W between Cape Mendocino and Point Arena, associated with the temperature front. These results seem credible given that the phenomenological behavior of the model simulation has been shown to be qualitatively similar to recent large-scale hydrographic, altimetric, drifter and moored observations of the CCS.

Acknowledgments

This work was supported by direct funding at the Naval Postgraduate School with the Office of Naval Research as the sponsor. We wish to thank the reviewers for comments which helped to improve the text. We also wish to thank Mike Cook for his computer assistance with Figs. 1 and 2, and Phaedra Green for editorial assistance.

References

Allen, J.S., Walstad, L.J., Newberger, P.A., 1991. Dynamics of the coastal transition zone jet, 2. Nonlinear finite-amplitude behavior. Journal of Geophysical Research 96, 14,995–15,016.

Arakawa, A., Lamb, V.R., 1977. Computational design of the basic dynamical processes of the UCLA general circulation model. In: Chang, J. (Ed.), Methods in Computational Physics, Academic Press, New York, vol. 17, pp. 173–265.

Auad, G., Pares-Sierra, A., Vallis, G.K., 1991. Circulation and energetics of a model of the California Current System. Journal of Physical Oceanography 21, 1334–1552.

Batteen, M.L., 1997. Wind-forced modeling studies of currents, meanders, and eddies in the California Current System. Journal of Geophysical Research 102, 985–1009.

Batteen, M.L., Collins, C.A., Gunderson, C.R., Nelson, C.S., 1995. The effect of salinity on density in the California Current System. Journal of Geophysical Research 100, 8733–8749.

Batteen, M.L., Butler, C.L., 1998. Modeling studies of the Leeuwin Current off Western and Southern Australia. Journal of Physical Oceanography, in press.

Batteen, M.L., Han, Y.-J., 1981. On the Computational noise of finite-difference schemes used in ocean models. Tellus 33, 387–396.

Batteen, M.L., Haney, R.L., Tielking, T.A., Renaud, P.G., 1989. A numerical study of wind forcing of eddies and jets in the California Current System. Journal of Marine Research 47, 493–523.

Batteen, M.L., Rutherford, M.J., Bayler, E.J., 1992. A numerical study of wind and thermal forcing effects on the ocean circulation off Western Australia. Journal of Physical Oceanography 22, 1406–1433.

Bernstein, R.L., Breaker, L.C., Whritner, R., 1977. California Current eddy formation: Ship, air, and satellite results. Science 195, 353–359.

Breaker, L.C., Mooers, C.N.K., 1986. Oceanic variability off the central California coast. Progress in Oceanography 17, 61–135.

Brink, K.H., Cowles, T.J., 1991. The coastal transition zone program. Journal of Geophysical Research 96, 14,637–14,647.

Camerlengo, A.L., O'Brien, J.J., 1980. Open boundary conditions in rotating fluids. Journal of Computational Physics 35, 12–35.

Chelton, D.B., 1984. Seasonal variability of alongshore geostrophic velocity off central California. Journal of Geophysical Research 89, 3473–3486.

Haidvogel, D.B., Beckman, A., Hedstrom, K.S., 1991. Dynamical simulation of filament formation and evolution in the coastal transition zone. Journal of Geophysical Research 96, 15,017–15,040.

Haney, R.L., 1974. A numerical study of the response of an idealized ocean to large-scale surface heat and momentum flux. Journal of Physical Oceanography 4, 145–167.

Haney, R.L., 1985. Midlatitude sea surface temperature anomalies: a numerical hindcast. Journal of Physical Oceanography 15, 787–799.

Hickey, B.M., 1979. The California Current System—Hypotheses and facts. Progress in Oceanography 8, 191–279.

Hickey, B.M., 1998. Western North America, Tip of Baja California to Vancouver Island. In: Robinson, Allan R. and Brink, Kenneth H., The Sea, Wiley, New York, pp. 345–393.

Holland, W.R., 1978. The role of mesoscale eddies in the general circulation of the ocean numerical experiments using a wind-driven quasigeostrophic model. Journal of Physical Oceanography 8, 363–392.

Holland, W.R., Batteen, M.L., 1986. The parameterization of subgrid scale heat diffusion in eddy-resolved ocean circulation models. Journal of Physical Oceanography 16, 200–206.

Holland, W.R., Harrison, D.E., Semtner, Jr. A.J., 1983. Eddy-resolving numerical models of large-scale ocean circulation. In: Eddies in Marine Science. Springer-Verlag, New York, pp. 379–403.

Huyer, A., Kosro, P.M., Fleischbein, J., Ramp, S.R., Stanton, T., Washburn, L, Chavez, F.P., Cowles, T.J., Pierce, S.D., Smith, R.L., 1991. Currents and water masses of the coastal transition zone off northern California, June to August 1988. Journal of Geophysical Research 96, 14,809–14,831.

Ikeda, M., Emery, W.J., 1984a. Satellite observations and modeling of meanders in the California Current system off Oregon and northern California. Journal of Physical Oceanography 14, 1434–1450.

Ikeda, M., Emery, W.J., Mysak, L.A., 1984b. Seasonal variability in meanders of the California current system off Vancouver Island. Journal of Geophysical Research 89, 3487–3505.

Ikeda, M., Mysak, L.A., Emery, W.J., 1984. Observations and modeling of satellite-sensed meanders and eddies off Vancouver Island. Journal of Physical Oceanography 14, 3–21.

Kelly, K.A., Beardsley, R.C., Lineburner, R., Brink, K.H., Paduan, J.D., Chereskin, T.K., 1998. Variability of near-surface eddy kinetic energy in the California Current based on altimetric, drifter, and moored current data. Journal of Geophysical Research, 103, 13 067–13 083.

Levitus, S.R., Burgett Boyer, T.P., 1994. World Ocean Atlas 1994, vol. 3: Salinity, NOAA Atlas NESDI 3. U.S. Department of Commerce, Washington, DC, 99 pp.

Levitus, S., Boyer, T.P., 1994. World Ocean Atlas 1994, vol. 4: Temperature. NOAA Atlas NESDI 4, U.S. Department of Commerce, Washington, DC, 117 pp.

Lynn, R.S., Simpson, J.J., 1887. The California Current System: The seasonal variability of its physical characteristics. Journal of Geophysical Research 92, 12,947–12,966.

Mooers, C.N.K., Robinson, A.R., 1984. Turbulent jets and eddies in the California Current and inferred cross-shore transports. Science 223, 51–53.

Narimousa, S., Maxworthy, T., 1985. Two-layer model of shear-driven coastal upwelling in the presence of bottom topography. Journal of Fluid Mechanics 159, 503–531.

Narimousa, S., Maxworthy, T., 1989. Application of a laboratory model to the interpretation of satellite and field observations of coastal upwelling. Dynamics of Atmospheres and Oceans 13, 1–46.

Nelson, C.S., Husby, D.M., 1983. Climatology of surface heat fluxes over the California current region. NOAA Technical Report NMFS SSRF-763, U.S. Department of Commerce, Washington, DC, 155 pp.

Pares-Sierra, A., White, W.B., Tai, C.K., 1993. Wind-driven coastal generation of annual mesoscale eddy activity in the California Current System: A numerical model. Journal of Physical Oceanography 23, 1110–1121.

Pierce, S.D., Allen, J.S., Walstad, L.J., 1991. Dynamics of the coastal upwelling zone jet, 1. Linear stability analysis. Journal of Geophysical Research 96, 14,979–14,993.

Simpson, J.J., Koblinsky, C.J., Haury, L.R., Dickey, T.D., 1984. An offshore eddy in the California Current System. Progress in Oceanography13, 1–111.

Strub, P.T., James, C., (1995) The Large-scale summer circulation of the California current. Geophysical Research Letters 22, 207–210.

Strub, P.T., Kosro, P.M., Huyer, A., CTZ Collaborators, 1991. The nature of the cold filaments in the California Current System. Journal of Geophysical Research 96, 14,743–14,768.

Walstad, L.J., Allen, J.S., Kosro, P.M., Huyer, A., 1991. Dynamics of the coastal transition zone through data assimilation studies. Journal of Geophysical Research 96, 14,959–14,977.

Trenberth, K.E., Large, W.G., Olson, J.G., 1990. The mean annual cycle in global ocean wind stress. Journal of Physical Oceanography 20, 1742–1760.

Weatherly, G.L., 1972. A study of the bottom boundary layer of the Florida Current. Journal of Physical Oceanography 2, 54–72.